Title

Crystal Crystal structure and mechanistic basis of a functional homolog of the antigen transporter TAP

Permalink

https://escholarship.org/uc/item/9n65v50m

Authors

Noll, A
Thomas, C
Hebring, V
et al.

Publication Date

2017

Peer reviewed

Crystal structure and mechanistic basis of a functional homolog of the antigen transporter TAP

Anne Nöll[a,1], Christoph Thomas[a,1], Valentina Herbring[a,1], Tina Zollmann[a], Katja Barth[a,b], Ahmad Reza Mehdipour[c], Thomas M. Tomasiak[d], Stefan Brüchert[a], Benesh Joseph[b], Rupert Abele[a], Vincent Oliéric[e], Meitian Wang[e], Kay Diederichs[f], Gerhard Hummer[c,g], Robert M. Stroud[d,2], Klaas M. Pos[a], and Robert Tampé[a,2]

[a]Institute of Biochemistry, Biocenter, Goethe University Frankfurt, 60438 Frankfurt am Main, Germany; [b]Institute of Physical and Theoretical Chemistry, Goethe University Frankfurt, 60438 Frankfurt am Main, Germany; [c]Theoretical Biophysics, Max Planck Institute of Biophysics, 60438 Frankfurt am Main, Germany; [d]Department of Biochemistry and Biophysics, University of California, San Francisco, CA 94158; [e]Swiss Light Source, Paul Scherrer Institute, 5232 Villigen PSI, Switzerland; [f]Molecular Bioinformatics, Department of Biology, University of Konstanz, 78457 Konstanz, Germany; and [g]Institute of Biophysics, Goethe University Frankfurt, 60438 Frankfurt am Main, Germany

ABC transporters form one of the largest protein superfamilies in all domains of life, catalyzing the movement of diverse substrates across membranes. In this key position, ABC transporters can mediate multidrug resistance in cancer therapy and their dysfunction is linked to various diseases. Here, we describe the 2.7-Å X-ray structure of heterodimeric *Thermus thermophilus* multidrug resistance proteins A and B (TmrAB), which not only shares structural homology with the antigen translocation complex TAP, but is also able to restore antigen processing in human TAP-deficient cells. TmrAB exhibits a broad peptide specificity and can concentrate substrates several thousandfold, using only one single active ATP-binding site. In our structure, TmrAB adopts an asymmetric inward-facing state, and we show that the C-terminal helices, arranged in a zipper-like fashion, play a crucial role in guiding the conformational changes associated with substrate transport. In conclusion, TmrAB can be regarded as a model system for asymmetric ABC exporters in general, and for TAP in particular.

ABC transporter | conformational dynamics | membrane proteins | peptide transport | transporter associated with antigen processing

ABC transporters use the energy of ATP binding and hydrolysis to translocate chemically diverse substrates across cell membranes, with substrates ranging from ions to lipids, peptides, and proteins (1–4). All ABC transporters are built from common structural modules comprising two nucleotide-binding domains (NBDs), which bind and hydrolyze ATP, and two transmembrane domains (TMDs) that facilitate substrate translocation (5, 6). Despite these common structural units, members of the different ABC protein subfamilies exhibit significant structural and mechanistic diversity (2). Based on the different organization of their structure and the direction of substrate translocation, ABC proteins can be classified into import and export systems. Although several structures of type-I ABC exporters in different states of the transport cycle have been solved, they are restricted to transporters with two canonic ATP-binding sites, with the exception of TM288/287 (7), whose transport activity is undefined.

Due to scarce structural and functional data on heterodimeric exporters, in which one half-transporter contributes to a catalytically inactive, degenerate ATP-binding site, our knowledge of heterodimeric transport systems is still incomplete. However, a better understanding of these systems is particularly important because a large number of the eukaryotic ABC transporters have nonequivalent nucleotide-binding sites, including the heterodimeric transporter associated with antigen processing TAP (8). The prevalence of heterodimeric ABC half-transporters suggests an underlying functional principle of NBD asymmetry (9–11). Apart from general unresolved aspects that concern all ABC exporters (i.e., the structural basis of substrate recognition and specificity as well as the trajectory of conformational changes associated with substrate translocation) there are major open questions that pertain to heterodimeric systems (e.g., how the interplay of the two non-equivalent NBDs is coupled to substrate transport).

To address these questions, we identified in a structural genomics screen a bacterial TAP homolog called TmrAB (*Thermus thermophilus* multidrug resistance proteins A and B), an obligatory heterodimeric ABC exporter, with one half-transporter, TmrB, contributing to the degenerate ATP-binding site (12). TmrAB was initially shown to be able to transport the fluorescent dye Hoechst 33342 and to be inhibited by verapamil (12). Because TmrAB is the only type-I ABC export complex in *T. thermophilus*, its substrate specificity is expected to be extremely broad. In fact, we recently demonstrated that phosphoglycolipids are bound to and released by TmrAB upon ATP hydrolysis, suggesting that this ABC transporter may also move lipids (13).

Here, we show that TmrAB is an exceptionally versatile ABC export system. In fact, TmrAB covers the substrate spectrum of the antigen translocation complex TAP and is able to fully restore antigen processing in TAP-deficient cells from immune-compromised patients; TmrAB can thus be regarded as a functional homolog of

Significance

ABC transporters shuttle chemically diverse substances across membranes in an energy-dependent manner. They mediate multidrug resistance in microorganisms and cancer cells and can cause human pathologies when dysfunctional. Although important insights into ABC transporters have been gained in recent years, fundamental questions concerning their mechanism remain open. Here, we identify the protein complex TmrAB as a functional homolog of the antigenic peptide transporter TAP and present its high-resolution structure. The structure adopts an asymmetric conformational state and is characterized by C-terminal zipper helices that are essential for efficient substrate translocation. The structure, together with functional studies, enables us to outline the general conformational dynamics of heterodimeric ABC transporters and to establish TmrAB as a model system for TAP.
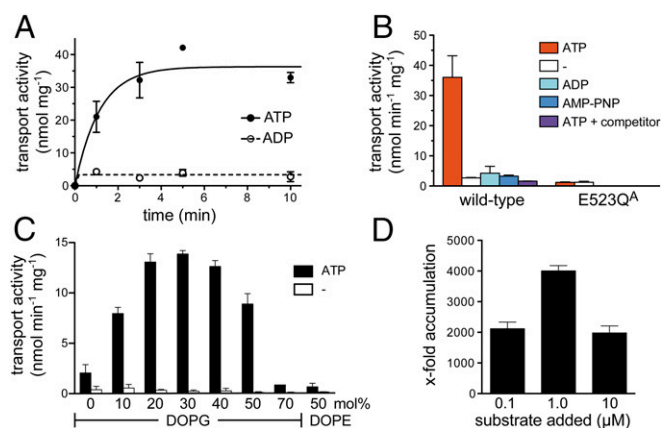
Fig. 1. Catalytic properties and broad substrate specificity of TmrAB. (*A*) Time course of ATP-dependent substrate transport (10 μM RRY^{FL}CKSTEL) by TmrAB at 68 °C. (*B*) Comparison of substrate (1 μM RRY^{3H}LKSTEL) transport by wild-type TmrAB and the hydrolysis-deficient mutant E523Q^A under varying conditions (15 min; competitor: 1 mM RRY^{FL}CKSTEL). (*C*) Modulation of TmrAB transport activity (3 μM RRY^{FL}CKSTEL, 20 min) by liposome lipid composition (P/L ratio of 1:200 wt/wt). The 1,2-dioleoyl-*sn*-glycero-3-phospholipids with various ratios of PG or PE to PC were analyzed. The different transport activities are related to similar amounts of reconstituted TmrAB. (*D*) Maximal substrate accumulation into liposomes catalyzed by TmrAB at different concentrations of RRY^{FL}CKSTEL. All data are given as mean ± SD (*n* = 3).

TAP. Determination of the crystal structure of TmrAB at 2.7-Å resolution, in combination with substrate transport and binding studies, allows us to identify the cavity formed by the TMDs as the substrate-discriminating region and to pin down a substrate-binding site. TmrAB adopts a unique asymmetric inward-facing conformation in our structure, with the NBDs positioned by C-terminal zipper helices that rearrange upon substrate translocation. We demonstrate that these zipper helices are essential for efficient transport. Supported by functional analyses, the structure enables us to derive the complete trajectory of conformational changes during the catalytic cycle of heterodimeric ABC transporters.

Results

Catalytic Properties and Broad Substrate Specificity.
To characterize the transport activity and substrate spectrum of TmrAB we reconstituted purified TmrAB into liposomes and performed fluorescence- and radioactivity-based transport assays with a range of different compounds. TmrAB displayed significant transport activity toward peptides [e.g., fluorescein (FL)-labeled RRY^{FL}CKSTEL (^{FL}peptide: V_{max} = 31.2 nmol min^{-1}·mg^{-1}, K_m = 8.3 μM) and tritiated RRY^{3H}LKSTEL (^{3H}peptide: V_{max} = 49.6 nmol min^{-1}·mg^{-1}, K_m = 361.2 μM)]. Transport was lost in the absence of ATP, in the presence of a competitor, or upon mutation of the catalytic glutamate in the NBD of TmrA (E523Q^A; Fig. 1 *A* and *B*). TmrAB also translocates FL (V_{max} = 5.1 nmol min^{-1}·mg^{-1}, K_m = 69.2 μM) (*SI Appendix, Table S1*), albeit less efficiently than peptides, judging by the k_{cat}/K_m ratio (^{FL}peptide: 8,434 M^{-1}·s^{-1}, ^{3H}peptide: 309 M^{-1}·s^{-1}, and FL: 190 M^{-1}·s^{-1}). The transport activity of TmrAB is modulated by the membrane lipid composition, with 30% phosphatidylglycerol (PG), a negatively charged phospholipid, being essential for activity in the context of zwitterionic phosphatidylcholine (PC) or phosphatidylethanolamine (PE) (Fig. 1*C*). Notably, TmrAB is able to concentrate substrates 4,000-fold in liposomes (Fig. 1*D*). This is particularly remarkable considering that heterodimeric TmrAB harbors only one functionally active nucleotide-binding site per complex and taking the chemical activity of the assay components, the ATP regeneration system, and a potential uncoupling by lipidic compounds into account.

Overall Structure of TmrAB. To explore the mechanism of substrate transport we determined the crystal structure of nucleotide-free TmrAB at a resolution of 2.7 Å by selenomethionine (SeMet) single-wavelength anomalous dispersion (SAD) phasing (Table 1). Because of the extreme unit-cell c dimension of 1,044 Å (space group: P6$_5$22; *SI Appendix, Fig. S1*), dedicated setups of the X-ray beam and detector had to be implemented for data collection (*Materials and Methods*). TmrAB is observed in an asymmetric inward-facing conformation that differs from other ABC transporter structures (*SI Appendix, Table S2*). The overall architecture of TmrAB exhibits two half-transporters interacting in an arrangement with pseudo-twofold symmetry (Fig. 2). The periplasmic gate is tightly sealed, preventing proton leakage. The substrate cavity is open to the cytoplasmic side, and the NBDs are separated; however, the NBDs are still in contact and positioned via their C-terminal helices (zipper helices), burying a total surface area of 1,498 Å^2. Apart from the cytoplasmic entry route, a lateral gate is formed by TmrB, which grants potential hydrophobic substrates access to the substrate cavity (Fig. 2*A*; see also the discussion of lipidic substrates below). This lateral gate is found only in TmrB, but not in TmrA, signifying the asymmetric architecture of TmrAB. Further notable structural differences between the two half-transporters are found in the A-loop of the NBDs and in periplasmic loop 1, which are significantly extended in TmrA (*SI Appendix, Fig. S2*). The cavity facilitating substrate translocation across the membrane is formed by the two TMDs, each comprising six transmembrane helices (TM1–6). Intra- and intersubunit TMD–NBD communication is organized by coupling helix 1 and 2 of each subunit (Fig. 2 *A* and *B*). The N-terminal elbow helices are located at the membrane–water interface. In our X-ray structure, we observe an arginine in each elbow helix (R17^A; R12^B) forming a salt bridge with an aspartate in TM6 (D332^A; D317^B; *SI Appendix, Fig. S3*). Notably, the residues involved in this interaction are conserved among ABC exporters, suggesting that they stabilize the heterodimeric complex as seen for TAP (14, 15). Comparing our X-ray structure of TmrAB with the cryo-EM model (16) shows

Table 1. Data collection and refinement statistics

| Data and statistics	SeMet-TmrAB	Native TmrAB
Data collection		
Space group	P6$_5$22	P6$_5$22
Unit-cell parameters, Å	a = 93.40, b = 93.40, c = 1,043.05	a = 93.37, b = 93.37, c = 1,043.95
Wavelength, Å	0.9791	1.0000
Resolution range, Å	48.88–3.60 (3.82–3.60)	48.91–2.70 (2.80–2.70)
Completeness, %	99.8 (99.2)	100.0 (100.0)
Redundancy	21.1 (20.3)	17.7 (11.7)
CC(1/2)	99.9 (70.1)	99.7 (27.6)
I/σ(I)	13.4 (1.8)	16.3 (0.9)
Refinement statistics		
No. of reflections (total/test)		77,034/3,853
R$_{work}$/R$_{free}$, %		22.6/27.2
No. of atoms		
Protein		9,291
Water		10
Sulfate		10
Mean B value, Å^2		106.8
Rms deviations		
Bond length, Å		0.008
Bond angle, °		1.14
Ramachandran (favored/allowed/disallowed), %		93.7/6.0/0.3
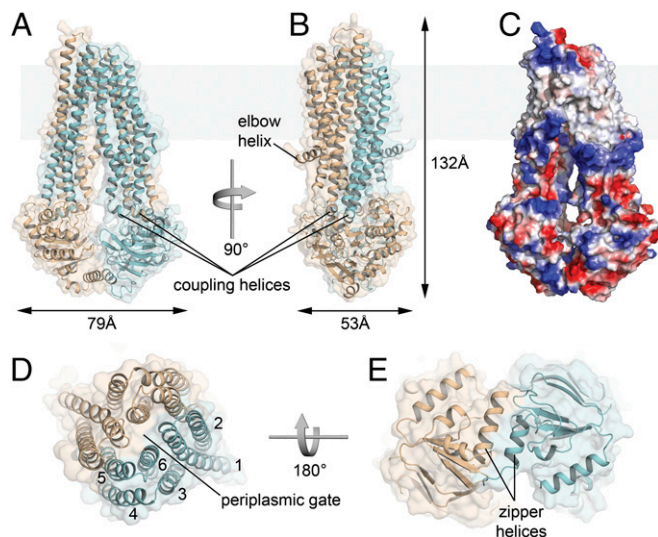
Fig. 2. Structure of the heterodimeric, asymmetric ABC transport complex TmrAB. (A and B) Ribbon representation of TmrA (wheat) and TmrB (cyan) in two different side-view orientations. The surface is shown as a transparent overlay. A faint gray bar depicts the membrane interface. (C) Electrostatic surface charge of TmrAB, revealing the hydrophobic transmembrane region of TmrAB. (D) View onto the TMDs from the periplasm, displaying the tightly closed periplasmic gate of the transporter. (E) Cytoplasmic view, showing the relative orientation of the two NBDs and their zipper helices.

a consistent conformation, with the X-ray model superimposable with the 8.2-Å EM density map. The average deviation of Cα positions is 2.4 Å, with a maximum deviation of 11.0 Å at the very C terminus of TmrB (*SI Appendix*, Fig. S4). The larger structural differences are found in several loop regions in both NBDs, in the C-terminal helix of TmrB, increasing linearly toward the terminus, and in the periplasmic loop; these are all regions that would be expected to be less defined in the lower-resolution model and could not be modeled accurately in the cryo-EM map. Furthermore, parts of TM6 of TmrA, as well as in TM2, TM4, and TM5 of TmrB, also showed some variability with regard to the crystal structure; however, TM4 or its equivalent has been observed to be

highly variable in several X-ray structures of ABC transporters (17–19). It is unclear whether the described differences between the cryo-EM model and the X-ray structure are due to a minor conformational change, caused by different experimental environments (cryo-EM vs. crystallography), or due to the limited resolution of the cryo-EM data.

TmrAB Restores Antigen Processing in Human TAP-Deficient Cells.
TmrAB shares 27–30% overall sequence identity with human TAP1 and TAP2, of which the TMDs account for 22% and the NBDs for 34% and 37%, respectively. We therefore wondered whether the bacterial TmrAB could restore TAP function in TAP1-negative skin fibroblast cells (BRE169) derived from an immune-compromised bare lymphocyte syndrome patient (20). We transfected the TAP1-deficient cells with TmrA and TmrB containing the extra domain TMD0 of TAP2 for the interaction with components of the MHC-I peptide-loading complex (Fig. 3A) (15, 21, 22). As expected, coreTAP1 (lacking its TMD0) can restore antigen processing by pairing with the endogenous TAP2 in TAP1-deficient cells, as evidenced by a significant increase in MHC-I surface expression (Fig. 3 B and C). Remarkably enough, TmrAB is also able to fully assume the function of TAP and restore MHC-I surface expression in the TAP-negative cells. Substitution of the catalytically active glutamate in TmrA (E523) blocked antigen processing and MHC-I surface expression to the level of mock- or untransfected cells. Noteworthily, TmrA or TmrB alone cannot rescue TAP function (Fig. 3C). These data demonstrate that TmrAB, in combination with the TMD0, can restore antigen presentation. TmrAB is therefore a full-fledged functional homolog of the TAP complex.

Substrate Selectivity by a Chemically Heterogeneous Binding Cavity.
We next addressed the substrate specificity and potential binding site. The inner surfaces of TMDs of TmrA and TmrB, forming the substrate-binding cavity, display considerable differences in their charge distribution (Fig. 4A), which might explain the ability of TmrAB to bind a range of chemically diverse substrates. The polyspecificity in substrate recognition is also reflected by the diverse physicochemical properties of the cavity residues contributed by TmrA and TmrB. Although the majority of conserved and invariant residues in the TMDs are located on the outside of the protein complex (*SI Appendix*, Fig. S5), TmrAB shares with TAP
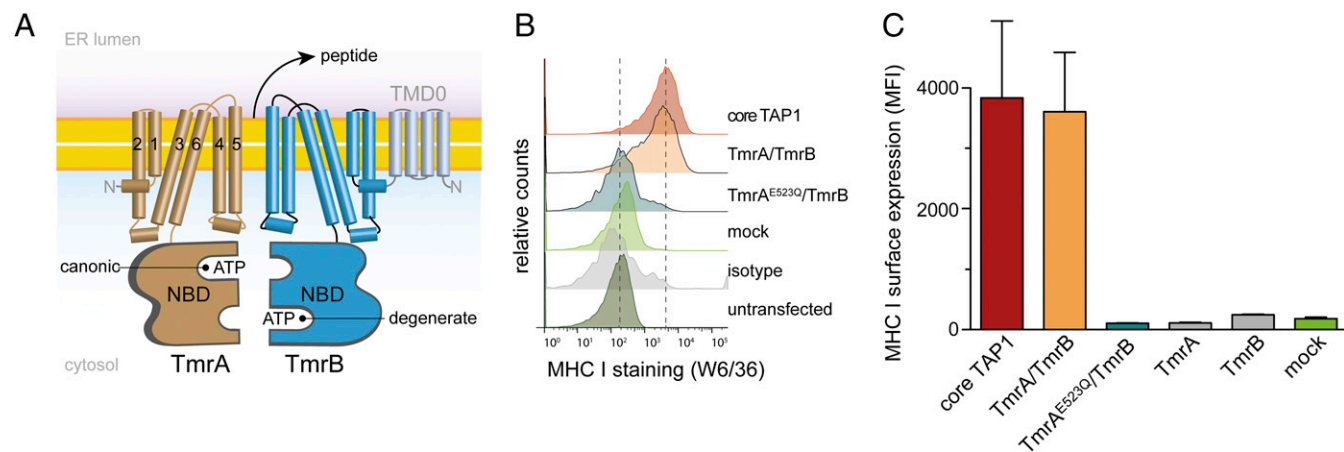

Fig. 3. TmrAB restores antigen processing in TAP-deficient cells. (A) The antigen translocation complex (coreTAP) and the bacterial TmrAB complex share structural and functional homology. TAP1/2 and TmrAB share one canonic, ATPase active and one degenerate nucleotide-binding site. TmrB was N-terminally fused to the TMD0 of TAP2 to promote the assembly of the MHC I peptide loading complex. (B) TmrAB restores antigen processing in TAP1-deficient cells from immune-compromised bare lymphocytes syndrome type-I patients. CoreTAP1 and TmrAB were expressed in BRE169 cells. Mutation of the catalytically active glutamate residue of TmrA to glutamine (E523Q) blocked antigen processing and MHC-I surface expression. MHC-I surface expression was monitored by the MHC I conformation-specific antibody W6/32. (C) Restoration of MHC I surface expression in TAP1-negative BRE169 cells by TmrAB. Mean fluorescence intensities (MFI ± SD) from at least three independent experiments are displayed.
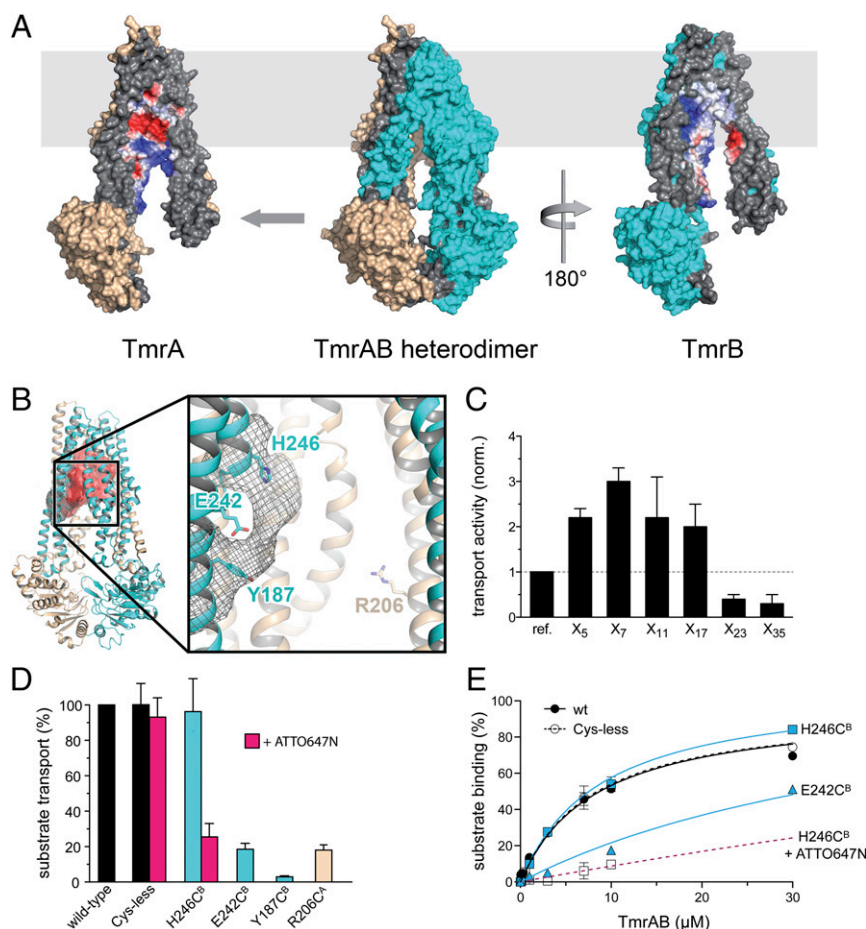
Fig. 4. A chemically heterogeneous binding cavity determines specificity. (*A*) Open-book representation of the TmrAB complex highlighting the different electrostatic surface charge distributions in the interior of TmrA and TmrB (gray, interface residues; red, negatively charged residues; blue, positively charged residues; and white, hydrophobic residues). (*B*) Overview of TmrAB, with the substrate-binding cavity shown in red, and close-up view of the cavity region. The extra EM density identified by cryo-EM and attributed to bound substrate is displayed as a gray mesh. Substituted residues are depicted as sticks. (*C*) Transport activity of TmrAB toward random-sequence ^{125}I-labeled peptides (3 μM) of different length (15-min values); reference peptide: RRYQKSTEL. (*D*) Transport activity of different TmrAB cavity mutants either unlabeled or labeled with ATTO647N-maleimide (magenta). (*E*) Substrate binding curves of label-free mutants TmrAB(E242C^B) and TmrAB(H246C^B), and of ATTO647N-labeled TmrAB(H246C^B). All data are given as mean ± SD (n = 3).

certain residues that have been shown to interact with peptide substrates in TAP. These include D297 in TAP1 (E131 in TmrB), identified by docking as part of a negatively charged pocket that contacts the peptide N terminus (23). Further peptide-interacting residues in TAP1 (24) shared with TmrB are G282, R287 (invariant G116^{TmrB} and R121^{TmrB}, respectively), I284 (L118^{TmrB}), and V288 (L122^{TmrB}). Moreover, particular residues that affect substrate specificity in TAP2 and may thus participate in substrate binding (25, 26) are either invariant (A374^{TAP2} and A258^{TmrA}) or physicochemically more or less conserved (N262^{TAP2} and Q146^{TmrA}; M218^{TAP2} and W100^{TmrA}). These common residues might at least partially explain the ability of TmrAB to take over the function of TAP in TAP-deficient cells.

For a more detailed analysis of the substrate-binding cavity, we defined the cavity as the inner region of TmrAB starting at the membrane–water interface and extending up to the periplasmic gate (Fig. 4*B*). Additional density in this region corresponding to putative substrate has been identified in the low-resolution cryo-EM map (Fig. 4*B*) (16). The cavity surface of TmrA is mainly charged, whereas it is predominantly hydrophobic in TmrB. Using random-sequence libraries of ^{125}I-labeled peptides, we determined the dependence of transport activity on substrate size. Although TmrAB was able to translocate polypeptides of 35 aa, 7-mer peptides were most efficiently transported (Fig. 4*C*). The upper

size limit is consistent with the volume of the cavity (5,760 Å^3). The optimal peptide length for TmrAB is similar to the one determined for TAP, which prefers peptides of 8–16 aa (27, 28). Considering the vast combinatorial diversity of the random-sequence peptide libraries, TmrAB exhibits remarkably versatile substrate specificity. The antigen translocation complex TAP is the only other ABC exporter for which such a broad peptide specificity with a similar length selectivity has been observed. In summary, TmrAB can be regarded as a bacterial prototype of the antigen translocation complex TAP, which plays a prominent role in adaptive immunity.

The high resolution of our X-ray structure in combination with site-directed mutagenesis allowed us to pinpoint specific residues involved in substrate binding and transport. We used the extra density identified in the cryo-EM study attributed to bound substrate as a starting point for mutational studies. This extra density bridges TM4 and TM5 in TmrB, close to residues Y187^B, E242^B, and H246^B (Fig. 4*B*). We substituted these residues in the immediate vicinity of the extra density to cysteine in Cys-less TmrAB and determined the transport activity of the mutants using the ^{FL}peptide. Whereas the H246C^B mutant displayed the same activity as the wild-type and the Cys-less complex, substitution of E242^B and Y187^B with Cys reduced the activity by 80–100% (Fig. 4*D*). To block the putative substrate-binding pocket, we coupled the spectrally unrelated fluorophore ATTO647N to the

cysteine of H246C[B]. Even though the H246C[B] mutant was not affected in its transport activity, coupling the bulky moiety to the cysteine resulted in a markedly lower activity.

To determine whether the reduced transport activities are due to impaired substrate recognition we directly measured substrate binding by fluorescence polarization (Fig. 4E). The E242C[B] mutant exhibited reduced substrate binding, suggesting that E242[B] is directly involved in binding of the [FL]peptide. An inhibition of substrate binding was observed if H246C[B] was labeled, indicating that the attached fluorophore obstructs access to the peptide-binding site. Furthermore, the cavity single-cysteine mutants H246C[B], E242C[B], and Y187C[B] are specifically disulfide cross-linked to a fluorescent peptide (*SI Appendix*, Fig. S6A). In contrast, the mutant R206C[A] (Fig. 4B) did not show any cross-linking (*SI Appendix*, Fig. S6A). Thus, part of the peptide-binding site seems to be located in the region of the extra EM density ascribed to a bound small-molecule compound, the same position where glutathione is bound to bacterial and mitochondrial Atm1-type ABC exporters (29, 30). Residues influencing transport activity but not directly involved in substrate binding, for example R206[A] (*SI Appendix*, Fig. S6B), most likely participate in the conformational changes that couple substrate binding and periplasmic gate opening.

Transport Pathway for Lipidic Substrates. In light of the fact that the activity of TmrAB is modulated by membrane lipids (Fig. 1C) and that TmrAB binds phospholipids and releases them upon ATP hydrolysis (13), we analyzed our structure with regard to potential lipid binding sites and translocation pathways: In addition to the cytosolic entry route to the substrate cavity, TM4 and TM6 of TmrB form a laterally open V-shaped gate that grants membrane-embedded substrates access to the substrate cavity (Figs. 2A and 3A). This entry point at the inner membrane leaflet is only present in TmrB, not in TmrA. In TmrB, five arginines (residue 177, 181, 185, 186, and 188) line the rim on one side of the lateral cleft. These arginines might facilitate the movement of phospholipids from the inner to the outer leaflet by providing a positively charged groove for the lipid headgroups, while leaving the hydrophobic lipid tails in the membrane. Molecular dynamics (MD) simulations with 1-palmitoyl-2-oleoyl-phosphatidylethanolamine (POPE) and 1-palmitoyl-2-oleoyl-phosphatidylglycerol (POPG), respectively, are consistent with this notion. We found that the arginine-enriched patch attracted a phospholipid molecule and retained it for the full duration of four independent simulations (GROMACS 2×2 μs, NAMD 2×0.5 μs; *SI Appendix*, Fig. S7). The tight fit of a lipid tail into the hydrophobic cleft between TM4 and TM6 further strengthens this interaction. Interestingly, MsbA, a homolog of TmrAB linked to lipid A translocation across the inner bacterial membrane (31, 32), has a similar cluster of positively charged residues in TM4 at the same position of the TMD, suggesting that this Arg/Lys cluster is a general feature of lipid-translocating ABC transporters. Clustered arginines have also been observed in the lipid-linked oligosaccharide flippase PglK (33); however, they lie in the interior of the cavity and have been proposed to interact with the pyrophosphate moiety of the substrate exclusively in the outward-facing state. This is in contrast to the role of the arginine cluster in TmrAB that we propose, which entails recruiting lipids at the inner membrane leaflet. MD simulations show that lipid A could fit into the substrate-binding cavity of TmrAB without any clashes (*SI Appendix*, Fig. S7), stabilized by strong electrostatic interactions with the headgroup and hydrophobic interactions with its six aliphatic tails. The two distinct binding modes seen in the simulations are consistent with lipid flippase activity. When the headgroup is clamped between R142[B]/R80[B] and R88[B]/R130[B], lipid A is orientated parallel to the membrane, as a flippase intermediate; trapped in the second clamp, formed by R142[B]/R80[B] and H246[B], lipid A points upward, as required for exterior release. The MD simulations are thus consistent with glycolipid release

upon ATP hydrolysis (13) and suggest a possible pathway for flipping and release.

Unzipping of C-Terminal Helices As an Essential Step of the Transport Cycle. In TmrAB, the NBD–NBD contacts mediated by the C-terminal helices are predominantly formed by van der Waals interactions between L572[B], L595[A], L565[B], and L602[A], packing in an arrangement similar to the "knobs-into-holes" pattern (Fig. 5A). We therefore refer to the C-terminal helices as "zipper helices." Polar contacts between the two helices are formed between Q598[A] and E568[B], between Y588[A] (main chain) and E575[B], and between R569[A], E575[B] (main chain), and the C-terminal carboxyl group of A578[B] (Fig. 5A). However, judging from the angles between hydrogen bond donors and acceptors, the interactions are rather weak. The lack of strong interactions might facilitate the movement of the two zipper helices relative to each other during the structural changes necessary to adopt the outward-facing conformation.

The contacting zipper helices of the NBDs in the TmrAB structure are in stark contrast to the inward-facing conformations of P-gp (17, 34, 35) and MsbA (36), which display extremely wide separations of their NBDs, or TM288/287 with almost closed NBDs (7). We analyzed the conformational dynamics and interaction between the zipper helices in the case of reconstituted TmrAB by disulfide cross-linking of an introduced cysteine pair (C416A,L595C[A]/E568C[B]) (Fig. 5B and *SI Appendix*, Fig. S8A). The resolution of our crystal structure allows us to design tailored cysteine substitutions at two opposite sites for cross-linking, with a Cα-Cα distance of 5.6 Å. Even though substrate binding was not affected (*SI Appendix*, Fig. S6B), the 100% cross-linked zipper variant did not show any transport activity (Fig. 5B), demonstrating that TmrAB has to undergo structural rearrangements during its catalytic cycle, involving unzipping of the C-terminal helices, that cannot be performed by the conformationally locked mutant. The fact that activity can be fully restored by reduction indicates that the loss of transport activity upon oxidation is not due to misfolded or damaged protein. Disulfide cross-linking of the C-terminal helices is significantly reduced when the mutant is vanadate-trapped in the
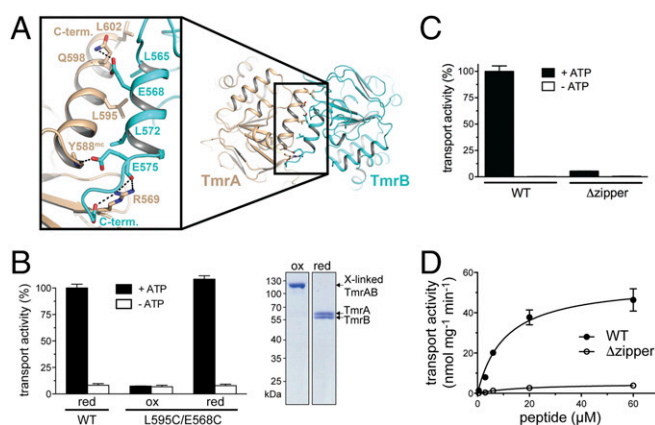

Fig. 5. The C-terminal zipper helices control the translocation cycle. (A) Details of the interaction between the C-terminal zipper helices of TmrA and TmrB in the NBDs (view from cytoplasm). Salt bridges and hydrogen bonds are shown as dotted lines. (B) Transport activity (1 μM RRY[FL]CKSTEL, 15-min values) of oxidized (ox) and reduced (red) C416A,L595C[A]/E568C[B]. Complete cross-linking upon oxidation is demonstrated by SDS/PAGE. (C) Transport activity of Δzipper TmrAB mutant, which lacks the C-terminal zipper helix of TmrA, in comparison with the wild-type protein (WT). (D) Transport kinetics of the wild-type and Δzipper TmrAB revealed a K_m value of 7.7 ± 1.0 μM and 12.5 ± 4.2 μM, respectively. All data are given as mean $\pm$ SD ($n = 3$).

hydrolytic transition state (*SI Appendix*, Fig. S8*B*), establishing that the zipper helices reorient during NBD closure.

The importance of the zipper helices was further analyzed by the deletion of the zipper helix in TmrA (Δzipper). Although the Δzipper complex presented the same expression level and purification profile as wild-type TmrAB, the transport activity of the Δzipper complex is significantly reduced (Fig. 5*C*). Nevertheless, the residual transport activity of the Δzipper complex allowed us to measure its transport kinetics (Fig. 5*D*). Despite the largely reduced turnover rate, the K_m value of the Δzipper complex for the transport substrate is similar to the wild-type protein (wild-type: $7.7 \pm 1.0 \mu M$; Δzipper: $12.5 \pm 4.2 \mu M$). Taken together, these results provide evidence for a role of the zipper helices as a functional motif in the TmrAB translocation cycle.

Opening and Closing of the Periplasmic Gate. In our structure, the periplasmic gate of TmrAB is closed, with several primarily hydrophobic side chains forming a tight seal that maintains the proton-motive force across the inner membrane. The opening of the periplasmic gate must be tightly coordinated if peptides, fluorophores, or potentially even lipids are released via this gate. We therefore examined the conformational change at the periplasmic gate of TmrAB during the transport cycle using pulsed electron-electron double resonance spectroscopy (PELDOR/DEER). Based on our X-ray structure, we strategically placed a spin-label pair at the periplasmic gate (Fig. 6*A*). We used vanadate to mimic the transition state in ATP hydrolysis and trap TmrAB in an outward-facing conformation. An analysis of this vanadate-trapped state

and the apo state gives evidence that the periplasmic gate of TmrAB opens by ~20 Å, from 20 to 40 Å, upon vanadate trapping (Fig. 6*B*). ADP and nonhydrolyzable AMP-PNP did not induce periplasmic gate opening (Fig. 6*C*), suggesting that formation of an ATP hydrolysis transition state is necessary to drive the change to the outward-facing conformation. Notably, due to the heterodimeric nature of TmrAB with a degenerate site, the hydrolytic transition state must be formed asymmetrically by the catalytically active site. The fact that the transition state is required to achieve the outward-facing state in the case of TmrAB is in contrast to the homodimeric transporters MsbA and Sav1866, where ATP and AMP-PNP, respectively, are sufficient to induce a similar conformational change (37, 38).

To assess the similarity between a detergent/lipid micellar environment and a lipid bilayer we determined the distances in TmrAB reconstituted in a lipid bilayer and obtained an opening of ~35 Å, from 20 to 55 Å (Fig. 6*D*). In the case of TmrAB, the surrounding lipid environment thus seems to significantly increase the extent of periplasmic gate opening in the transition state. The transition to the outward-facing state in TmrAB was strictly dependent on vanadate trapping, similar to the case with BmrCD (9), suggesting that the formation of the hydrolytic transition state may be the balance point in the ATP hydrolysis-driven power stroke in heterodimeric ABC transport complexes.

Discussion

TmrAB is a highly efficient transporter that can concentrate substrate several thousandfold. Moreover, it exhibits a remarkably
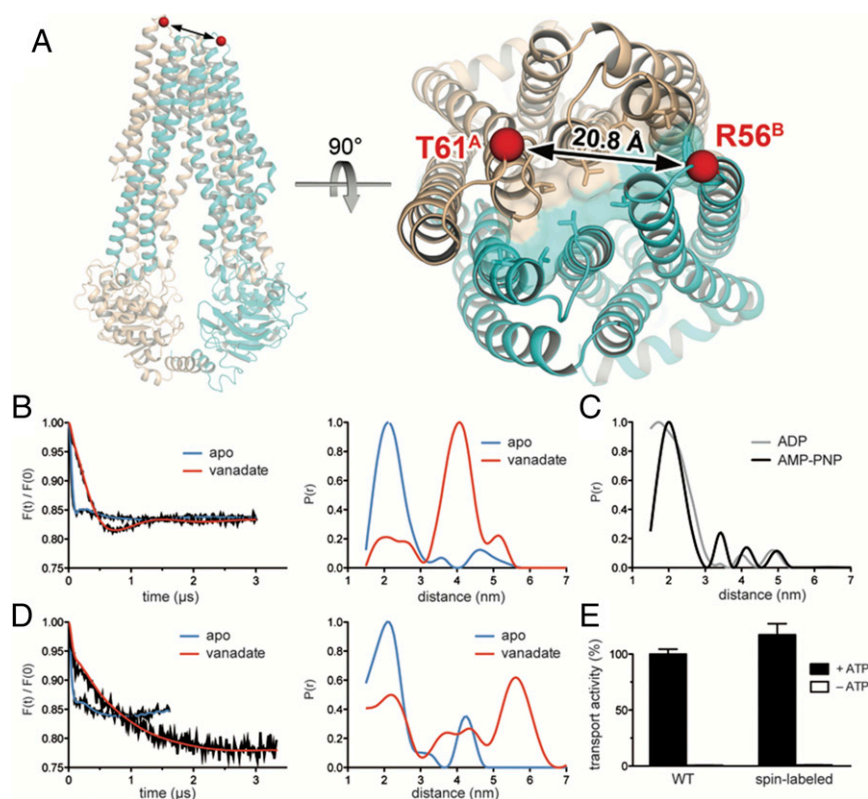

Fig. 6. Conformational dynamics of the periplasmic gate probed by EPR. (*A*) Positions of residues (Cα atoms shown as red spheres) in TmrA and TmrB that were mutated to cysteine and modified with the spin label MTSSL. Residues of the closed periplasmic gate are presented with their surface. (*B*) Pulsed electron-electron double resonance (PELDOR/DEER) spectroscopy of double-spin-labeled C416A,T61C[A]/R56C[B] in apo and vanadate-trapped state reveals that in the vanadate-trapped state the periplasmic gate opens by ~20 Å in detergent and by ~35 Å in liposomes. Normalized Q-band PELDOR traces were corrected for intermolecular background function applying a monoexponential fit to obtain the form factors (*Left*). Distance distributions were calculated using Tikhonov regularization with the DeerAnalysis software (58). PELDOR measurements carried out with detergent-solubilized (*B* and *C*) and membrane-reconstituted TmrAB (*D*). (*E*) Spin-labeled TmrAB displays similar transport activity as the wild-type complex. Data are given as mean ± SD (*n* = 3).

broad substrate specificity that fully covers the substrate spectrum of the human antigenic peptide transporter TAP, as exemplified by its ability to rescue MHC I surface presentation in TAP-deficient cells. TmrAB can be distinguished from TAP by its capacity to recognize fluorophores (FL), to be inhibited by verapamil (12), and its possible function as a lipid translocator (13). Despite the high activity, we noted that the transport rate and ATP turnover (12) are not identical. However, a defined 1:1 or 1:2 ratio of transported substrate per ATP has not yet been observed for any ABC export system. This could be explained by (*i*) a cotransport of lipidic compounds and (*ii*) the possibility that not all of our TmrAB complexes are transport-active after reconstitution, as has been demonstrated for the TAP-like complex by single-liposome-based analysis (39).

Although a comprehensive understanding of the activity of ABC transport complexes will only result from high-resolution structures of several different on-pathway intermediates of the same protein and of substrate-bound complexes, the current structure provides insights into the inner workings of this important protein family at the molecular and atomic level and hence suggests models of substrate transport by TmrAB. As outlined above, our crystal structure of TmrAB differs significantly from previously determined X-ray structures of *Thermotoga maritima* TM288/287 [Protein Data Bank (PDB) ID code 4Q4A] and *Staphylococcus aureus* Sav1866 (PDB ID code 2HYD) (11, 40). This allowed us to derive a trajectory of conformational changes associated with the transport cycle of ABC exporters. Whereas TM288/287 represents an inward-facing intermediate with a maximum of one occluded nucleotide, Sav1866 is in an outward-facing state with two fully occluded nucleotide-binding sites. The movement of the two NBDs relative to each other during the translocation cycle is accompanied by a successive reorientation of the Walker A motif (P-loop) relative to the signature motif of the opposite NBD (Fig. 7*A* and Movie S1). The distance between Walker A (P-loop; conserved lysine) and signature motif (C-loop; conserved serine) decreases from TmrAB (Cα distance K399^A–S476^B: 24.9 Å; K377^B–S498^A: 24.3 Å) over TM288/287 (Cα distance for both K394^{288}–S471^{287}: 18.1 Å; K372^{287}–S493^{288}: 17.2 Å) to Sav1866 (Cα distance for K380-S479 between the two protomers: 9.5 Å). In Sav1866, the two NBDs have adopted a closed dimer state; the relative movement of Walker A and signature motif has been brought to completion, positioning the signature motif in the immediate vicinity of the Walker A motif and tightly packing the two nucleotides between the NBDs.

Another striking structural change along the trajectory from the inward- to the outward-facing conformation is the movement of the catalytic glutamate (E523^A) (Fig. 7*A* and Movie S1). In apo TmrA, this glutamate, which acts as a catalytic base polarizing the water molecule that attacks the ATP (canonic site), is oriented away from the catalytically active nucleotide-binding site (Fig. 7*A*). In the nucleotide-occluded Sav1866 structure, however, the glutamate has moved into a hydrolysis-competent position. With regard to the position of its rearranged zipper helices, the TM288/287 structure resembles the Sav1866 structure, whereas the periplasmic gate is closed, that is, the arrangement of the TM helices is similar to TmrAB (Fig. 7*B*). The structural changes in the NBDs of TM288/287 seem to be not sufficiently advanced on the conformational trajectory to induce periplasmic gate opening.

During the transition from the inward- to the outward-facing conformation of TmrAB the overall rearrangement of the NBDs consists of translational motions (Movie S1). These motions require the C-terminal zipper helices to unzip and to switch their positions (Fig. 7*C*). Our experiments demonstrate that the zipper helices are essential for an efficient catalytic transport cycle. The C-terminal zipper helices of yeast Atm1 show an arrangement similar to that in TmrAB. However, in Atm1-type transporters, these helices are significantly longer and interact in a slight cross-over as opposed to antiparallel fashion (29, 30). C-terminal deletion mutants of Atm1
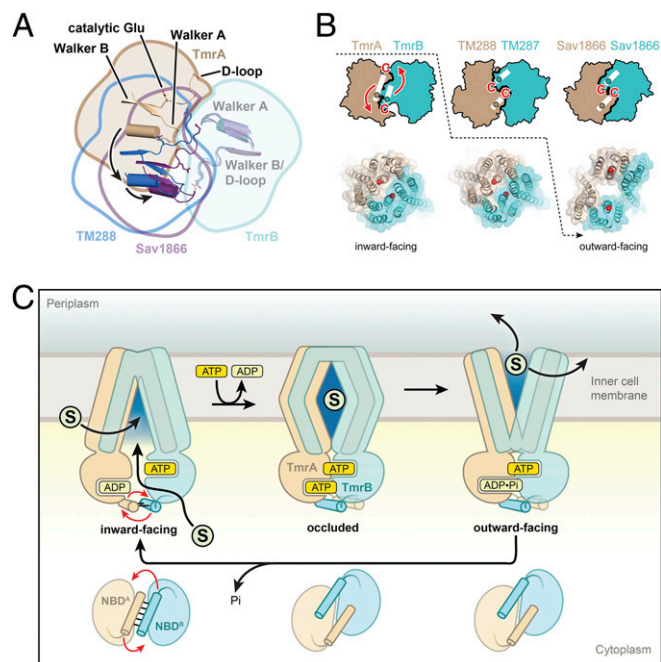

Fig. 7. Conformational dynamics of TmrAB and the catalytic transport cycle. (*A*) Relative movement of the NBDs during the transport cycle, analyzed by superimposing the NBDs of TmrB (pale cyan), TM287, and of one Sav1866 protomer; P-loop, Walker B, and D-loop of the superimposed NBDs are shown in transparent colors. Structural elements of the NBD moving relative to the superimposed domains are depicted in opaque colors. (*B*) Structural side-by-side comparison of TmrAB with alternating conformations displayed by TM288/287 and Sav1866. (*Top*) Schematic outline of the NBDs with the positions of the C-terminal helices highlighted by white rectangles. The relative positions of the two C-terminal helices are marked by a wheat and cyan dot. The red arrows indicate the movement of the two C-terminal helices. The red C stands for the C terminus. (*Bottom*) View onto the TMDs from the periplasmic side showing the closed state of the periplasmic gate in TmrAB and TM288/287, and the open state in Sav1866. The Cα atoms of two glycines are shown as red spheres (G291 in TmrA and G276 in TmrB, and corresponding positions in TM288/287 and Sav1866). (*C*) Model of substrate transport by TmrAB and the role of the zipper helices. TmrAB (subunits shown as schematic outlines) is able to transport a diverse range of substrates (depicted as encircled letter "S"), both soluble and membrane-associated compounds. An arginine cluster in TmrB at the rim of the lateral gate mediates association with headgroups of lipidic substrates. The inward-facing state with juxtaposed NBDs is stabilized by interactions between the C-terminal zipper helices. ATP and substrate binding induce a conformational transition to an occluded state, in which the NBDs interact intimately, but the periplasmic gate is still closed. For this transition, the zipper helices must dissolve their interaction and switch their position. The central cavity (shown in dark blue) functions as the cargo compartment that mediates substrate transport from the cytoplasmic to the periplasmic side of the membrane. ATP hydrolysis leads to periplasmic gate opening, allowing the substrate to leave the cavity. Release of phosphate restores the inward-facing state of TmrAB.

were interpreted as suggesting that they affected primarily stability rather than function because lowered activity was accompanied by substantially lower expression. We propose that the zipper helices position the NBDs and act as checkpoints that allow the transporter to execute its conformational transitions in a coherent and productive manner. They might also help the transporter to avoid the extremely large NBD separations that have been observed for some ABC exporters (e.g., P-gp, MsbA, and PglK) (17, 33–36). It remains to be determined how common this role of the C-terminal helices is among ABC transporters.

Conformational changes in the NBDs are allosterically coupled to a reorganization of the TMDs. This reorganization is most pronounced in regions of TM4 and TM6 that form the lateral entrance gate. At the base of the gate, the two TM helices are

separated by a distance of 12.5 Å ($D184^B$–$A300^B$ Cα distance) in TmrB. In the outward-facing conformation of Sav1866, the lateral gate is blocked by TM4 and TM6, and the substrate cavity is exposed to the extracellular space and the outer leaflet of the membrane. Between the inward- and outward-facing states there is an intermediary putative occluded state (Fig. 7C), similar to the ones that have been observed in the substrate-free structures of the homodimeric ABC exporters McjD and PCAT1 (41, 42).

A pivotal role in transmitting conformational changes between NBDs and TMDs during substrate transport has been assigned to coupling helices in the NBD–TMD interfaces (40, 43, 44). They are a common feature of ABC transporters. In TmrAB, the interactions in the NBD–TMD interfaces are mainly TmrAB-specific (*SI Appendix*, Fig. S9); one notable exception is a triad of interacting Arg, Asp, and Tyr residues that can also be found in *Caenorhabditis elegans* and *Cyanidioschyzon merolae* ABCB1, TM288/287, and ABCB10 (7, 17, 18, 45). The high degree of conservation suggests that this motif may fulfill an important function in the communication between NBDs and TMDs. Certain regions of the transmembrane helices seem to contribute to the structural flexibility necessary to carry out the conformational changes accompanying substrate transport; these regions might be thought of as hinges and may even act as a trigger, coupling substrate binding to periplasmic gate opening. The region with the highest mobility in TmrAB is indeed located in TM6 of TmrA right above the elbow helix and spans roughly 16 aa (residues 304–319). The weak electron density in this region, which includes a proline and glycine, reflects its high mobility. A similar feature has been observed in the corresponding helix (TM12) of *C. elegans* P-gp (17), and it has been suggested that the flexibility is functionally important in mediating substrate interactions and/or transducing conformational changes induced by substrate binding and substrate occlusion (17, 41). Helical irregularities in TM6 close to the substrate-binding site have also been observed in Atm1-type transporters (29, 30). In summary, these findings substantiate the idea that discontinuous transmembrane helices are a common attribute of many transport proteins.

In its ability to transport a diverse set of peptides, drugs, and lipophilic compounds, TmrAB seems to be a member of the TAP/MDR subfamily of transporters, which translocate a wide range of compounds and for which loss-of-function mutations have been linked to various diseases. In this respect, the structure of TmrAB may open new avenues to therapeutic intervention, especially in the case of mammalian ABC transporters, many of which are characterized by an asymmetric organization of the central cavity as well as a functional nonequivalence of the NBDs as in TmrAB. Moreover, the particular ability of TmrAB to fully substitute the TAP complex functionally suggests that TmrAB can serve as a model system for TAP, a key component of antigen processing in adaptive immunity.

Materials and Methods

Cloning and Expression. TmrA (TTC0976) and tmrB (TTC0977) were PCR-amplified from *T. thermophilus* HB27 genomic DNA. Wild-type TmrAB as well as the ATPase inactive complex $TmrA^{E523Q}$/TmrB were cloned as described previously (12). Cysteine mutants were prepared by site-directed mutagenesis. Both wild-type and mutant proteins were expressed in *Escherichia coli* BL21(DE3) as described (12). SeMet-labeled protein was prepared using Selenomethionine Expression Media (Molecular Dimensions).

Protein Purification. Protein purification was performed at 4 °C unless stated differently. Harvested *E. coli* cells were resuspended in lysis buffer (20 mM Hepes and 300 mM NaCl, pH 7.5) containing lysozyme (Sigma) and DNase I (Applichem). Cells were disrupted using an automated French press (1.0 kbar, Basic Z; Constant Systems) and cell debris was removed by centrifugation at $10,000 \times g$ for 15 min. The supernatant was centrifuged at $120,000 \times g$ for 1 h to pellet membranes. Membranes were solubilized with solubilization buffer [20 mM Hepes, 300 mM NaCl, pH 7.5, and 20 mM *n*-dodecyl-β-ᴅ-maltopyranoside (β-DDM; Anatrace)] to a final concentration of 40 mg/mL total protein and incubated for 1 h at 20 °C. Detergent-solubilized protein was separated by

centrifugation at $100,000 \times g$ for 30 min. His-tagged TmrAB was bound to Ni-NTA agarose (Qiagen) equilibrated with purification buffer (20 mM Hepes, 300 mM NaCl, pH 7.5, 30 mM imidazole (pH 8.0), and 1 mM β-DDM) and washed with purification buffer containing 50 mM imidazole and 1 mM β-mercaptoethanol. Protein was eluted with purification buffer supplemented with 300 mM imidazole. Fractions containing TmrAB were desalted by Econo-Pac10DG (Bio-Rad) columns equilibrated in SEC buffer (20 mM Hepes, 150 mM NaCl, pH 7.2, and 1 mM β-DDM). The His tag was cleaved by tobacco etch virus (TEV) protease treatment. Cleaved protein was separated from TEV protease by reverse immobilized-metal affinity chromatography using Ni-NTA agarose in size-exclusion chromatography (SEC) buffer. TmrAB was purified via SEC using a TSK G3000SW column (Tosoh Bioscience LLC) in SEC buffer. The main fractions of the monodisperse peak were pooled for crystallization. The mutants were purified using the same protocol, except for the double-cysteine mutant $TmrA^{C416A,L595C}$/$TmrB^{E568C}$. In this case, 1 mM of β-mercaptoethanol was added to all buffers to prevent oxidation. Oxidative cysteine cross-linking was induced by buffer exchange to SEC buffer without β-mercaptoethanol via an Econo-Pac 10DG column at 20 °C.

Crystallization. Before crystallization, TmrAB was concentrated to 23 mg/mL by ultrafiltration using a 50-kDa molecular weight cutoff Amicon Ultra-0.5 (Millipore). TmrAB crystals were obtained by the vapor diffusion method in hanging drops at 18 °C against a reservoir containing 26–30% PEG 400, 0.1 M Na_3citrate/HCl, pH 3.5, 0.1 M Li_2SO_4, and 0–2.5 mM CYMAL-5. Concentrated TmrAB containing 5 mM AMP-PNP and 5 mM $MgCl_2$ was mixed with reservoir solution in a 1:1 volume ratio. Crystals appeared after 1–3 d and were grown for another 5–12 d until they reached their full size of 0.2–0.5 mm. Crystals were directly flash-frozen in liquid nitrogen without additional cryoprotectant. SeMet-labeled TmrAB was crystallized under the same conditions, but at 12 °C.

Data Collection. Diffraction data of native and SeMet-labeled TmrAB crystals were collected at beamline X06SA of the Swiss Light Source. Because of an extremely long unit cell axis (unit-cell dimensions: a = b = 93.4 Å, c = 1,044.0 Å; space group: $P6_522$) (*SI Appendix*, Fig. S1 and Table 1), a special beamline setup was necessary. X-ray optics were adjusted to focus the beam on the detector surface to minimize diffraction spot size and so eliminate overlaps. The X-ray beam size was defined with slits to 100×100 μm² at the sample position to match the average size of TmrAB crystals. Diffraction patterns were recorded to 2.7 Å with a PILATUS 6M, while maintaining good separation of the densely spaced diffraction spots. The resulting sharp diffraction spots also helped to increase the signal-to-noise ratio for weak reflections at high resolution. In addition, crystal orientation was manipulated to have the long unit cell axis close to the rotation spindle axis to avoid spot overlaps during rotation data collection. Native data were collected to 2.7 Å resolution at a wavelength of 1.0000 Å, whereas SeMet data were collected to 3.6 Å resolution at a wavelength of 0.9793 Å. Diffraction data were processed with the program XDS (46). Minimum distances allowed between spots and maximum radius of difference vector clusters were adjusted manually (SEPMIN = 2 and CLUSTER_RADIUS = 1) to allow indexing of the closely spaced reflections arising from the 1,044-Å axis. The crystals belong to space group $P6_522$, containing one TmrAB heterodimer per asymmetric unit.

Structure Determination. Initial phases were obtained by SAD using SeMet derivative crystals (*SI Appendix*, Fig. S10). The heavy atom substructure of 19 selenium atoms was determined by SHELXD and initial phases were obtained using SHELXE (47). This yielded an interpretable electron density map. Automatic chain tracing using Buccaneer v1.5 (48) was used as an initial guide for building an intermediate polyalanine model, which was refined against the native dataset using PHENIX v1.9 (49). Based on the asymmetry in methionine distribution, the two protomers could be distinguished from the SeMet substructure. The chains of TmrA and TmrB were traced, and the model was built using Coot v0.8 (50) and refined using PHENIX. The high-resolution limit was chosen based on paired refinement calculations (51) at different cutoffs and found to give the best model and electron density. The complete polypeptide chains of TmrAB were built with the exception of 10 N-terminal residues (1–10) of TmrA. $Phe314^A$ was substituted by alanine because of ill-defined density for the side chain. Analysis of the crystal lattice showed that the crystal contacts are mainly restricted to parts of the NBDs and residues of the periplasmic loops. All molecular graphics and the morph were prepared using PyMOL (Schrödinger, LLC). The substrate cavity was calculated using the 3v server (52). Structural superpositions were carried out using the program SSM (53). To analyze the extra EM density in the context of our crystal structure, the volume eraser tool in Chimera was used to remove some of the micelle density to have an unobstructed view into the cavity. The subsequent superposition was carried out using the range Tyr187–His246 in TmrB. Root-mean-square deviation values

were determined in PyMOL using the align command with the parameter cycles = 0. The align command carries out a sequence alignment before structural superposition.

Restoration of Antigen Processing by TmrAB in TAP-Negative Cells. *TmrA* and *tmrB* were transferred to a mammalian expression system. TmrA was cloned into pcDX c3YCH and TmrB into pcDX (54). The TMD0 of human TAP2 (residues 1–127) was added seamlessly at the N terminus of TmrB. All cloning steps were based on PCR amplification by *Pfu* DNA polymerase and FX-cloning (55). TAP1-deficient BRE169 cells (20) were transfected with TmrA, TmrB, coreTAP1 (15), or empty pcDX c3YCH as mock according to the X-treme-GENE HP manual. Forty-eight hours after transfection, cells were harvested and stained with PE anti-human HLA-A,B,C (clone W6/32; BioLegend). Cells were fixed with 0.25% formaldehyde. Data were recorded by a FACSAria III 3 sorter (BD Bioscience) flow cytometer and processed using FlowJo 10 software (TreeStar, Inc.).

Reconstitution into Liposomes. Liposomes composed of *E. coli* polar lipids/DOPC (7:3) or mixture of phospholipids plus 5 mol % *E. coli* cardiolipin (Avanti Polar Lipids) with a total lipid concentration of 10 mg/mL prepared in reconstitution buffer [20 mM Hepes, pH 7.5, 140 mM NaCl, and 5% (vol/vol) glycerol] were extruded 11 times through a 400-nm polycarbonate filter. After destabilizing the liposomes for 30 min at 4 °C with Triton X-100 (Roth), SEC-purified TmrAB was added at a protein-to-lipid ratio of 1:20 (wt/wt) unless stated differently and incubated for 30 min at 4 °C. Detergent was removed in a stepwise fashion over a period of 20 h using Bio-Beads (Bio-Rad). Proteoliposomes were pelleted by ultracentrifugation at $270,000 \times g$ for 30 min at 4 °C. Pelleted proteoliposomes were resuspended in reconstitution buffer to a final lipid concentration of 5 mg/mL. The reconstitution efficiency was confirmed either by vesicle pelleting or carbonate crush (100 mM Na_2CO_3, pH 11.5), followed by liposome floating assay using sucrose density centrifugation [0, 20, and 30% (wt/vol) sucrose, $228,000 \times g$ for 1 h at 4 °C] and analyzed by SDS/PAGE (10%, silver stain).

Peptide Transport. Proteoliposomes (final 1 mg/mL lipid) were incubated with 3 mM $MgCl_2$, 3 mM nucleotides, and substrates in transport buffer [20 mM Hepes, pH 7.5, 107 mM NaCl, and 5% (vol/vol) glycerol] at 68 °C for different time periods. Reactions were stopped by adding four volumes of ice-cold stop buffer (1× PBS and 10 mM EDTA). Samples were transferred to a polyethyleneimine-coated Multi Screen Filter Plate (Durapore membrane 0.65 μm; Millipore) and washed twice with five volumes of stop buffer. Liposomes were lysed with lysis buffer (1× PBS and 0.1% SDS) for 10 min. Fluorescent substrates were transferred to a microtiter plate and fluorescence was quantified using an ELISA reader (FLUOstar Galaxy BMG) ($\lambda_{ex/em}$ 485/520 nm). Transport assays with radiolabeled substrates were performed under similar conditions. For ^{125}I-labeled substrates, filters were cut and measured by γ counting (COBRAII; Packard). For ^{3}H-labeled substrates, filters were cut and each sample was incubated with 1 mL scintillation solution (Rotiszint eco plus LSC-universal mixture; Roth). Readout was performed in a LS6500 liquid scintillation counter (Beckman). Data are presented as means ± SD ($n = 3$). Peptides were synthesized on solid-phase using Fmoc chemistry and labeled via cysteine with iodoacetamido FL (RRY^{FL}CKSTEL). Final products were purified by reversed-phase C_{18} HPLC. Peptide identity was confirmed by electrospray ionization MS. Leucine [4,5-^{3}H] was incorporated by solid-phase peptide synthesis. Iodination of peptides with ^{125}I was carried out using a chloramine-T-based method (56).

Substrate Accumulation. For peptide accumulation in proteoliposomes, a creatine kinase-based ATP-regenerating system (ARS) is required to sustain the driving force during long-term transport experiments. As reference for the total liposomal volume, Alexa647-labeled dextran (dextran^{Alexa647}; Invitrogen) was encapsulated during lipid film rehydration of the liposome preparation. The dextran^{Alexa647} concentration was kept at 50 μM during liposome preparation and the whole TmrAB reconstitution procedures. Dextran^{Alexa647}-loaded TmrAB proteoliposomes were further washed with reconstitution buffer and a second harvesting step ($270,000 \times g$, 30 min, 4 °C) was carried out to remove external dextran^{Alexa647}. ^{FL}peptide accumulation was performed in a total volume of 500 μL with proteoliposomes (50 μg protein) at a protein-to-lipid ratio of 1:20 (wt/wt) at 45 °C for 2 h in ARS transport buffer [20 mM Hepes, pH 7.5, 5% (vol/vol) glycerol, 42.5 mM NaCl, 0.3 mg/mL creatine kinase, 24 mM phosphocreatine sodium salt, and 3 mM $MgSO_4$], adding 0.1, 1.0, or 10 μM of ^{FL}peptide. The reaction was started by adding ATP (3 mM final) and stopped after the indicated times by addition of 500 μL ice-cold stop buffer. Samples were transferred and treated as described for substrate transport. The amount of transported substrate was quantified by a fluorescence spectrometry (Cary Eclipse; Varian) at $\lambda_{ex/em}$ = 492/517 nm (FL) in relation to the internal volume measured by the amount of fluorescent dextran at $\lambda_{ex/em}$ = 650/668 nm (Alexa647). Samples without ATP were used as negative control and subtracted as background. Data are presented as means ± SD ($n = 3$).

Substrate Binding. Binding of fluorescently labeled substrates was analyzed by fluorescence polarization. A total sample volume of 20 μL in a 384-well format was chosen to minimize the protein consumption. ^{FL}peptide (50 nM) was titrated with increasing concentration of TmrAB in SEC buffer. The measurement was performed at 20 °C using Infinite 200 PRO multimode reader (Tecan). Each sample was measured as triplicate and presented as means ± SD. Data were fitted by a Langmuir (1:1) isotherm.

Fluorophore Labeling. The purified single-cysteine TmrA^{C416A}/TmrB^{H246C} complex was labeled with a 40-fold molar excess of ATTO647N-maleimide (Invitrogen) for 2 h at 20 °C in SEC buffer. Free fluorophore was removed by SEC using a PD-10 desalting column (GE Healthcare). The labeling efficiency of TmrA^{C416A}/TmrB^{H246C} was determined using SDS/PAGE, followed by in-gel fluorescence ($\lambda_{ex/em}$ = 630/670 nm) using a fluorescence imager (ImageQuant LAS 4000; GE Healthcare).

Pulsed Electron-Electron Double Resonance (PELDOR/DEER) Spectroscopy. TmrA^{C416A,T61C}/TmrB^{R56C} was labeled with a 40-fold molar excess of (1-oxyl-2,2,5,5-tetramethylpyrroline-3-methyl)-methanethiosulfonate spin label (MTSSL) at 25 °C for 30 min in buffer containing 20 mM Hepes, pH 7.5, 150 mM NaCl, and 1 mM β-DDM. Free spin probes were removed by Micro Bio-Spin 6/30 (Bio-Rad) centrifugation. A labeling efficiency of 90–100% was determined by spin counting using 4-amino-2,2,6,6-tetramethyl-piperidinyloxyl as reference. TmrAB was reconstituted as described above. Spin-labeled TmrAB displays the same transport activity as wild type. EPR experiments were performed without nucleotides (apo state) or with Mg-ATP, Mg-ADP, Mg-AMP-PNP, or Mg-ATP and vanadate (10 mM each). For PELDOR, 10 μL of sample containing 15–20% deuterated glycerol was transferred into a 1.6-mm-outer-diameter quartz EPR tubes (Suprasil; Wilmad LabGlass). All PELDOR data were recorded on an ELEXSYS E580 EPR spectrometer (Bruker) equipped with a PELDOR unit (E580-400U; Bruker), a continuous-flow helium cryostat (CF935; Oxford Instruments), and a temperature control system (ITC 502; Oxford Instruments). Pulsed experiments were performed at Q-band frequencies (33.7 GHz) using an ELEXSYS SuperQ-FT accessory unit and a Bruker AmpQ 10-W amplifier with a Bruker EN5107D2 cavity at 50 K. The dead-time free four-pulse sequence with phase-cycled π/2-pulse was used (57). Thereby, typical pulse lengths for the observer pulses were 32 ns (π/2 and π) and 20 ns (π) for the pump pulse, which was set to the maximum of the echo-detected field swept spectrum, the observer pulses being set 60 MHz lower. Deuterium modulations were averaged by increasing the first interpulse delay by 16 ns for eight steps. For determination of distance distributions, the software DeerAnalysis (58) was used, in which the normalized PELDOR data V(t)/V(0) were processed to remove the background function arising from intermolecular interactions and the resulting form factors F(t)/F(0) were fitted with a model-free Tikhonov regularization to distance distributions.

1. Rees DC, Johnson E, Lewinson O (2009) ABC transporters: The power to change. *Nat Rev Mol Cell Biol* 10(3):218–227.
2. Locher KP (2016) Mechanistic diversity in ATP-binding cassette (ABC) transporters. *Nat Struct Mol Biol* 23(6):487–493.
3. Davidson AL, Chen J (2004) ATP-binding cassette transporters in bacteria. *Annu Rev Biochem* 73:241–268.
4. Higgins CF (2007) Multiple molecular mechanisms for multidrug resistance transporters. *Nature* 446(7137):749–757.
5. Schmitt L, Tampé R (2002) Structure and mechanism of ABC transporters. *Curr Opin Struct Biol* 12(6):754–760.
6. Higgins CF (1992) ABC transporters: From microorganisms to man. *Annu Rev Cell Biol* 8:67–113.
7. Hohl M, Briand C, Grütter MG, Seeger MA (2012) Crystal structure of a heterodimeric ABC transporter in its inward-facing conformation. *Nat Struct Mol Biol* 19(4):395–402.
8. Parcej D, Tampé R (2010) ABC proteins in antigen translocation and viral inhibition. *Nat Chem Biol* 6(8):572–580.

9. Mishra S, et al. (2014) Conformational dynamics of the nucleotide binding domains and the power stroke of a heterodimeric ABC transporter. *eLife* 3:e02740.

10. Grossmann N, et al. (2014) Mechanistic determinants of the directionality and energetics of active export by a heterodimeric ABC transporter. *Nat Commun* 5:5419.

11. Hohl M, et al. (2014) Structural basis for allosteric cross-talk between the asymmetric nucleotide binding sites of a heterodimeric ABC exporter. *Proc Natl Acad Sci USA* 111(30):11025–11030.

12. Zutz A, et al. (2011) Asymmetric ATP hydrolysis cycle of the heterodimeric multidrug ABC transport complex TmrAB from *Thermus thermophilus*. *J Biol Chem* 286(9):7104–7115.

13. Bechara C, et al. (2015) A subset of annular lipids is linked to the flippase activity of an ABC transporter. *Nat Chem* 7(3):255–262.

14. Koch J, Guntrum R, Tampé R (2005) Exploring the minimal functional unit of the transporter associated with antigen processing. *FEBS Lett* 579(20):4413–4416.

15. Koch J, Guntrum R, Heintke S, Kyritsis C, Tampé R (2004) Functional dissection of the transmembrane domains of the transporter associated with antigen processing (TAP). *J Biol Chem* 279(11):10142–10147.

16. Kim J, et al. (2015) Subnanometre-resolution electron cryomicroscopy structure of a heterodimeric ABC exporter. *Nature* 517(7534):396–400.

17. Jin MS, Oldham ML, Zhang Q, Chen J (2012) Crystal structure of the multidrug transporter P-glycoprotein from *Caenorhabditis elegans*. *Nature* 490(7421):566–569.

18. Kodan A, et al. (2014) Structural basis for gating mechanisms of a eukaryotic P-glycoprotein homolog. *Proc Natl Acad Sci USA* 111(11):4049–4054.

19. Szewczyk P, et al. (2015) Snapshots of ligand entry, malleable binding and induced helical movement in P-glycoprotein. *Acta Crystallogr D Biol Crystallogr* 71(Pt 3):732–741.

20. de la Salle H, et al. (1999) HLA class I deficiencies due to mutations in subunit 1 of the peptide transporter TAP1. *J Clin Invest* 103(5):R9–R13.

21. Hulpke S, Tampé R (2013) The MHC I loading complex: a multitasking machinery in adaptive immunity. *Trends Biochem Sci* 38(8):412–420.

22. Blees A, et al. (2015) Assembly of the MHC I peptide-loading complex determined by a conserved ionic lock-switch. *Sci Rep* 5:17341.

23. Lehnert E, et al. (2016) Antigenic peptide recognition on the human ABC transporter TAP resolved by DNP-enhanced solid-state NMR spectroscopy. *J Am Chem Soc* 38(42):13967–13974.

24. Herget M, et al. (2007) Mechanism of substrate sensing and signal transmission within an ABC transporter: Use of a Trojan horse strategy. *J Biol Chem* 282(6):3871–3880.

25. Baldauf C, Schrodt S, Herget M, Koch J, Tampé R (2010) Single residue within the antigen translocation complex TAP controls the epitope repertoire by stabilizing a receptive conformation. *Proc Natl Acad Sci USA* 107(20):9135–9140.

26. Armandola EA, et al. (1996) A point mutation in the human transporter associated with antigen processing (TAP2) alters the peptide transport specificity. *Eur J Immunol* 26(8):1748–1755.

27. van Endert PM, et al. (1994) A sequential model for peptide binding and transport by the transporters associated with antigen processing. *Immunity* 1(6):491–500.

28. Androlewicz MJ, Cresswell P (1994) Human transporters associated with antigen processing possess a promiscuous peptide-binding site. *Immunity* 1(1):7–14.

29. Lee JY, Yang JG, Zhitnitsky D, Lewinson O, Rees DC (2014) Structural basis for heavy metal detoxification by an Atm1-type ABC exporter. *Science* 343(6175):1133–1136.

30. Srinivasan V, Pierik AJ, Lill R (2014) Crystal structures of nucleotide-free and glutathione-bound mitochondrial ABC transporter Atm1. *Science* 343(6175):1137–1140.

31. Doerrler WT, Reedy MC, Raetz CR (2001) An *Escherichia coli* mutant defective in lipid export. *J Biol Chem* 276(15):11461–11464.

32. Zhou Z, White KA, Polissi A, Georgopoulos C, Raetz CR (1998) Function of *Escherichia coli* MsbA, an essential ABC family transporter, in lipid A and phospholipid biosynthesis. *J Biol Chem* 273(20):12466–12475.

33. Perez C, et al. (2015) Structure and mechanism of an active lipid-linked oligosaccharide flippase. *Nature* 524(7566):433–438.

34. Li J, Jaimes KF, Aller SG (2014) Refined structures of mouse P-glycoprotein. *Protein Sci* 23(1):34–46.

35. Aller SG, et al. (2009) Structure of P-glycoprotein reveals a molecular basis for polyspecific drug binding. *Science* 323(5922):1718–1722.

36. Ward A, Reyes CL, Yu J, Roth CB, Chang G (2007) Flexibility in the ABC transporter MsbA: Alternating access with a twist. *Proc Natl Acad Sci USA* 104(48):19005–19010.

37. Borbat PP, et al. (2007) Conformational motion of the ABC transporter MsbA induced by ATP hydrolysis. *PLoS Biol* 5(10):e271.

38. Dawson RJ, Locher KP (2007) Structure of the multidrug ABC transporter Sav1866 from Staphylococcus aureus in complex with AMP-PNP. *FEBS Lett* 581(5):935–938.

39. Zollmann T, et al. (2015) Single liposome analysis of peptide translocation by the ABC transporter TAPL. *Proc Natl Acad Sci USA* 112(7):2046–2051.

40. Dawson RJ, Locher KP (2006) Structure of a bacterial multidrug ABC transporter. *Nature* 443(7108):180–185.

41. Choudhury HG, et al. (2014) Structure of an antibacterial peptide ATP-binding cassette transporter in a novel outward occluded state. *Proc Natl Acad Sci USA* 111(25):9145–9150.

42. Lin DY, Huang S, Chen J (2015) Crystal structures of a polypeptide processing and secretion transporter. *Nature* 523(7561):425–430.

43. Cotten JF, Ostedgaard LS, Carson MR, Welsh MJ (1996) Effect of cystic fibrosis-associated mutations in the fourth intracellular loop of cystic fibrosis transmembrane conductance regulator. *J Biol Chem* 271(35):21279–21284.

44. Currier SJ, et al. (1992) Identification of residues in the first cytoplasmic loop of P-glycoprotein involved in the function of chimeric human MDR1-MDR2 transporters. *J Biol Chem* 267(35):25153–25159.

45. Shintre CA, et al. (2013) Structures of ABCB10, a human ATP-binding cassette transporter in apo- and nucleotide-bound states. *Proc Natl Acad Sci USA* 110(24):9710–9715.

46. Kabsch W (2010) Xds. *Acta Crystallogr D Biol Crystallogr* 66(Pt 2):125–132.

47. Sheldrick GM (2010) Experimental phasing with SHELXC/D/E: Combining chain tracing with density modification. *Acta Crystallogr D Biol Crystallogr* 66(Pt 4):479–485.

48. Cowtan K (2006) The Buccaneer software for automated model building. 1. Tracing protein chains. *Acta Crystallogr D Biol Crystallogr* 62:1002–1011.

49. Adams PD, et al. (2010) PHENIX: A comprehensive Python-based system for macromolecular structure solution. *Acta Crystallogr D Biol Crystallogr* 66:213–221.

50. Emsley P, Lohkamp B, Scott WG, Cowtan K (2010) Features and development of Coot. *Acta Crystallogr D Biol Crystallogr* 66(Pt 4):486–501.

51. Karplus PA, Diederichs K (2012) Linking crystallographic model and data quality. *Science* 336(6084):1030–1033.

52. Voss NR, Gerstein M (2010) 3V: Cavity, channel and cleft volume calculator and extractor. *Nucleic Acids Res* 38(Web Server issue):W555-62.

53. Krissinel E, Henrick K (2004) Secondary-structure matching (SSM), a new tool for fast protein structure alignment in three dimensions. *Acta Crystallogr D Biol Crystallogr* 60(Pt 12 Pt 1):2256–2268.

54. Hinz A, et al. (2014) Assembly and function of the major histocompatibility complex (MHC) I peptide-loading complex are conserved across higher vertebrates. *J Biol Chem* 289(48):33109–33117.

55. Geertsma ER, Dutzler R (2011) A versatile and efficient high-throughput cloning tool for structural biology. *Biochemistry* 50(15):3272–3278.

56. Hunter WM, Greenwood FC (1962) Preparation of iodine-131 labelled human growth hormone of high specific activity. *Nature* 194:495–496.

57. Jeschke G (2012) DEER distance measurements on proteins. *Annu Rev Phys Chem* 63:419–446.

58. Jeschke G, et al. (2006) DeerAnalysis2006 – A comprehensive software package for analyzing pulsed ELDOR data. *Appl Magn Reson* 30:473–498.

Supporting Information

Nöll et al. 10.1073/pnas.1620009114
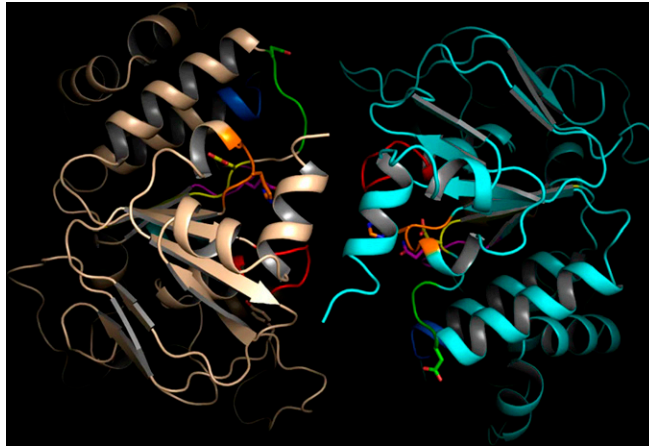
Movie S1.   Structural interconversion between the inward- and outward-facing conformations of TmrAB. Using PyMOL, a morph was calculated between the inward-facing structure of TmrAB and a homology model based on the outward-facing state of Sav1866. Characteristic structural elements of the NBDs are highlighted in different colors: P-loop (Walker A), red; D-loop, green; signature motif, blue; Walker B, yellow; Q-loop, magenta; and H-switch, orange.

[Movie S1](#)

Other Supporting Information Files

[SI Appendix (pdf)](#)

Supplemental Information

Crystal structure and mechanistic basis of a functional homolog of the antigen transporter TAP

Anne Nöll[a,1], Christoph Thomas[a,1], Valentina Herbring[a,1], Tina Zollmann[a],
Katja Barth[a,b], Ahmad Reza Mehdipour[c], Thomas M. Tomasiak[d], Stefan Brüchert[a],
Benesh Joseph[b], Rupert Abele[a], Vincent Olieric[e], Meitian Wang[e], Kay Diederichs[f],
Gerhard Hummer[c,g], Robert M. Stroud[d], Klaas M. Pos[a], and Robert Tampé[a,2]

[a]Institute of Biochemistry, Biocenter, [b]Institute of Physical and Theoretical
Chemistry, Goethe University Frankfurt, Max-von-Laue-Str. 9, 60438 Frankfurt am
Main, Germany; [c]Theoretical Biophysics, Max Planck Institute of Biophysics, Max-
von-Laue-Str. 3, 60438 Frankfurt am Main, Germany; [d]Department of Biochemistry
and Biophysics, University of California San Francisco, 600 16th Street, San
Francisco, CA 94158, USA; [e]Swiss Light Source at Paul Scherrer Institute, 5232
Villigen PSI, Switzerland; [f]Molecular Bioinformatics, Department of Biology,
University of Konstanz, 78457 Konstanz, Germany; [g]Institute of Biophysics, Goethe
University Frankfurt, 60438 Frankfurt am Main, Germany.

[1] A.N., C.T. and V.H. contributed equally to this work.

[2] To whom correspondence should be addressed. Email: tampe@em.uni-frankfurt.de

Supplementary Table

Table S1. Kinetic parameters of TmrAB for different substrates

	Carboxy-fluorescein	RRY^{FL}CKSTEL	RRY^{3H}LKSTEL
$K_{m,substate}$ (µM)	69.2 ± 3.6	8.3 ± 1.7	361.2 ± 40.9
V_{max} (nmol min^{-1} mg^{-1})	5.1 ± 0.1	31.2 ± 1.8	49.6 ± 2.4
k_{cat} (min^{-1})	0.79 ± 0.01	4.2 ± 0.2	6.7 ± 0.3
k_{cat}/K_m (M^{-1} s^{-1})	190	8434	309

RRY^{FL}CKSTEL: fluorescein-labeled peptide, RRY^{3H}LKSTEL: tritiated peptide. The data are derived from measurements that were carried out at 68 °C for 3 min with 3 mM of Mg-ATP and 2.5 µg of TmrAB in 50 µg *E. coli* polar lipids/DOPC (7:3), buffer: 20 mM HEPES pH 7.5, 107 mM NaCl, 5% glycerol.

Table S2. Root-mean-square deviations of Cα positions between TmrAB and other ABC transporter structures

| ABC transporter	PDB ID	resolution (Å) / R$_{free}$	Cα rmsd (Å)
TM287/288	3QF4	2.9 / 0.263	6.5
Cm-ABCB1	3WMG	2.4 / 0.246	9.4
ABCB10	4AYW	3.3 / 0.286	6.7
	3ZDQ	2.9 / 0.244	7.3
	4AYT	2.9 / 0.248	8.6
Na-Atm1	4MRN	2.5 / 0.227	9.5
Sc-Atm1	4MYC	3.1 / 0.298	9.4
Sav1866	2HYD	3.0 / 0.272	8.7
mouse P-gp	4M1M	3.8 / 0.266	9.1
MsbA	3B5X	5.5 / 0.360	6.9
	3B60	3.7 / 0.343	9.2
PCAT1	4RY2	3.6 / 0.289	12.2
Ce-P-gp	4F4C	3.4 / 0.283	13.0
McjD	4PL0	2.7 / 0.266	15.7
PglK	5C78	2.9 / 0.267	20.1

Supplementary Figures
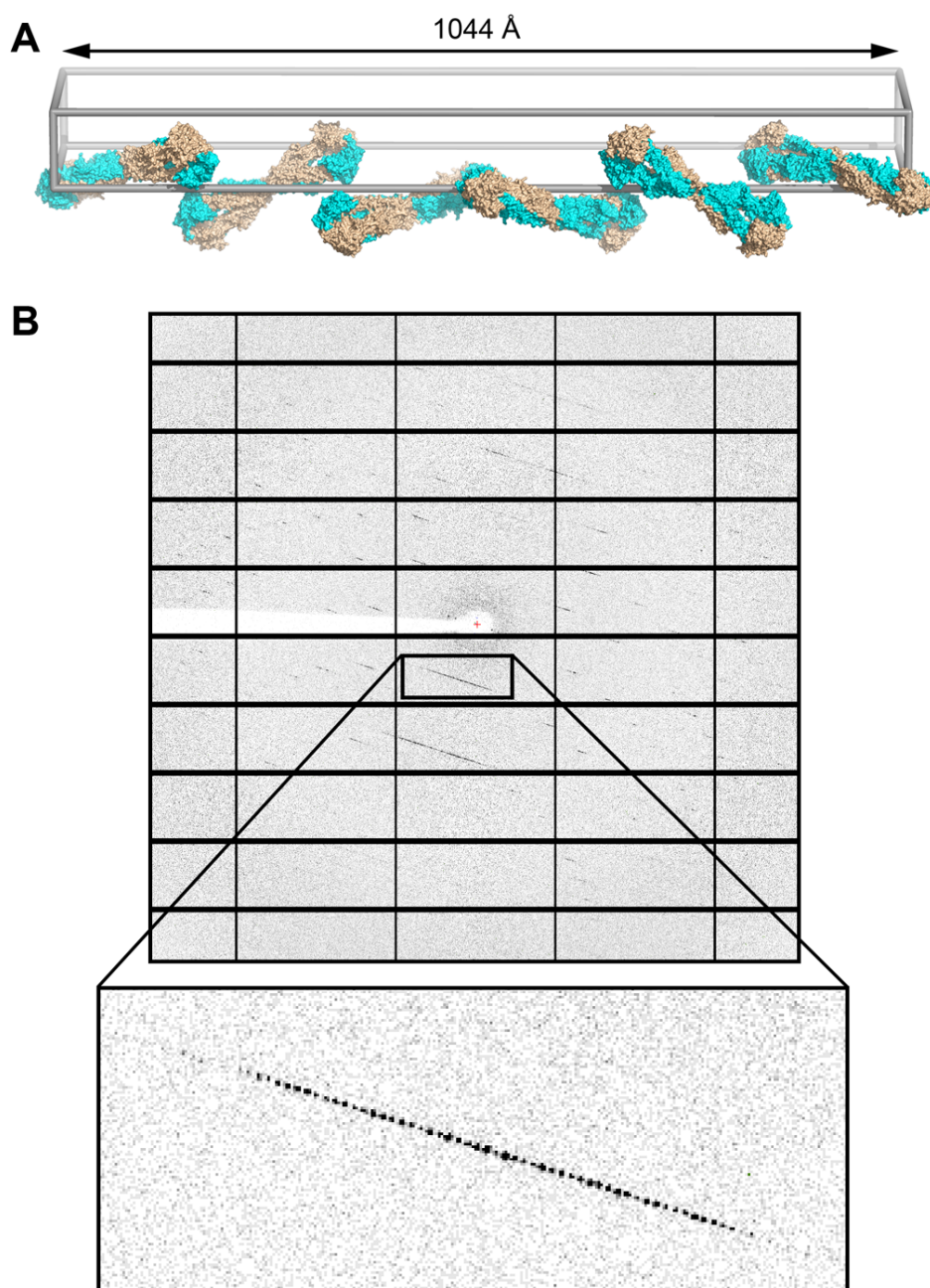
Fig. S1. Crystallographic features of TmrAB. (*A*) Crystals of TmrAB are characterized by an extremely long unit cell axis of 1044 Å. The unit cell is shown in grey with protein molecules depicting the symmetry elements of the space group. (*B*) Representative X-ray diffraction image of a TmrAB crystal. The long unit cell axis results in extreme narrowly spaced diffraction spots.
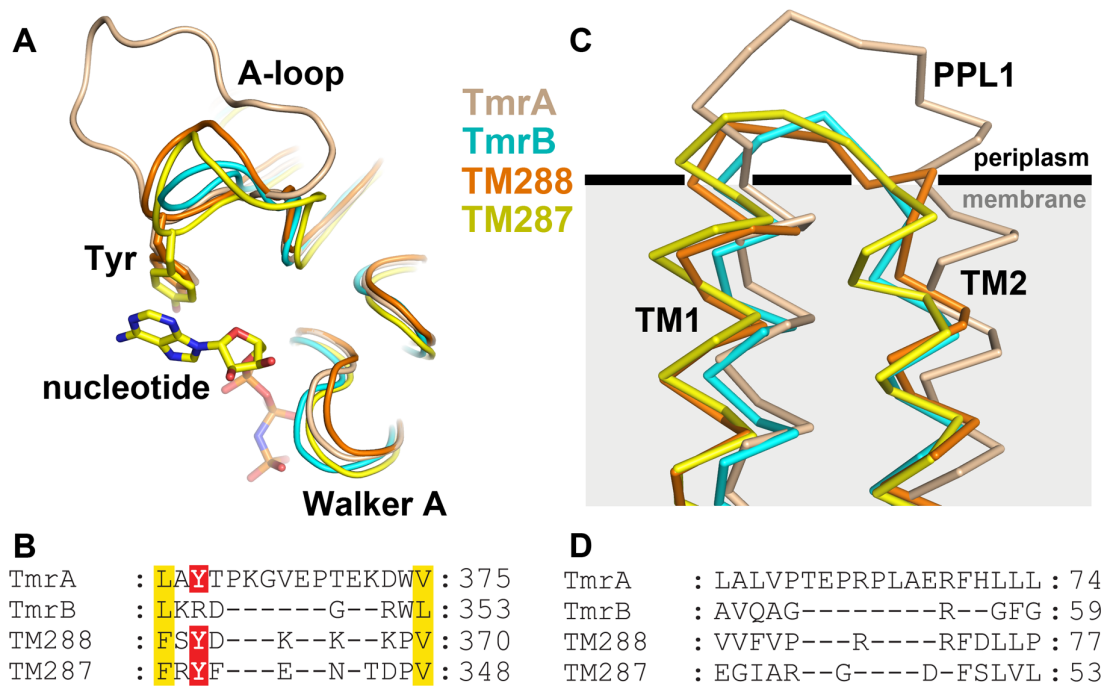
Fig. S2. Structural asymmetry in extended loops. (*A*) Superposition of nucleotide-binding regions of TmrA, TmrB, TM288, and TM287 (PDB code 4Q4A) highlighting the extended A-loop in TmrA. (*B*) ClustalW multiple sequence alignment of the A-loop region. The conserved A-loop Tyr, which is an arginine in the non-canonical nucleotide-binding site of TmrB, is shown in red, physicochemically conserved residues in yellow. (*C*) Structural comparison of the periplasmic loop 1 (PPL1) between TM1 and TM2 in TmrA, TmrB, TM288, and TM287. (*D*) Sequence alignment of the PPL1 region.
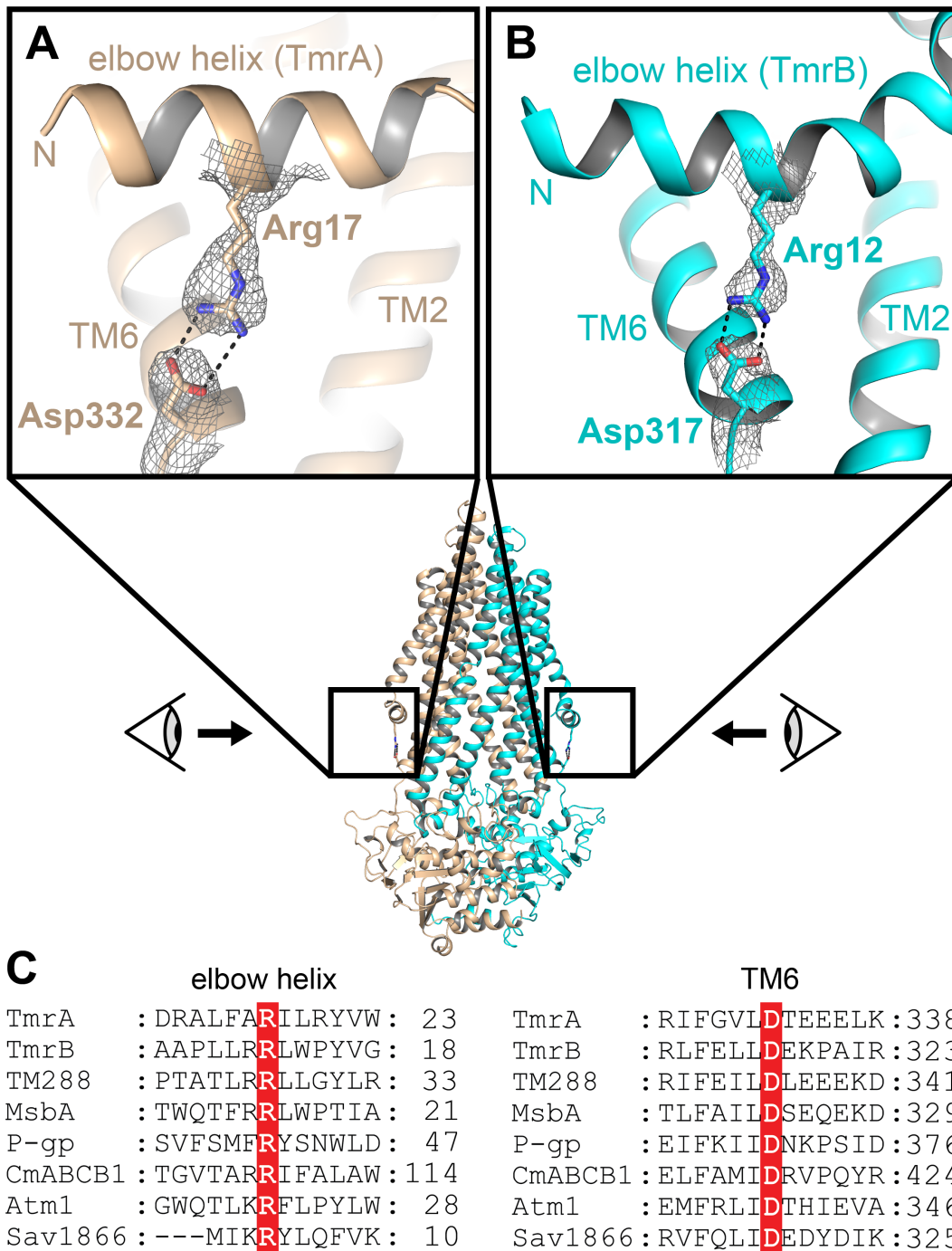
Fig. S3. Conserved salt bridge between elbow helix and TM6. (*A, B*) Conserved Arg-Asp salt bridge in TmrA and TmrB, respectively. Salt-bridge residues are shown with the corresponding section of the 2Fo-Fc map contoured at 0.8σ. (*C*) ClustalW multiple sequence alignment of different ABC transporters highlighting the invariant salt-bridge residues.
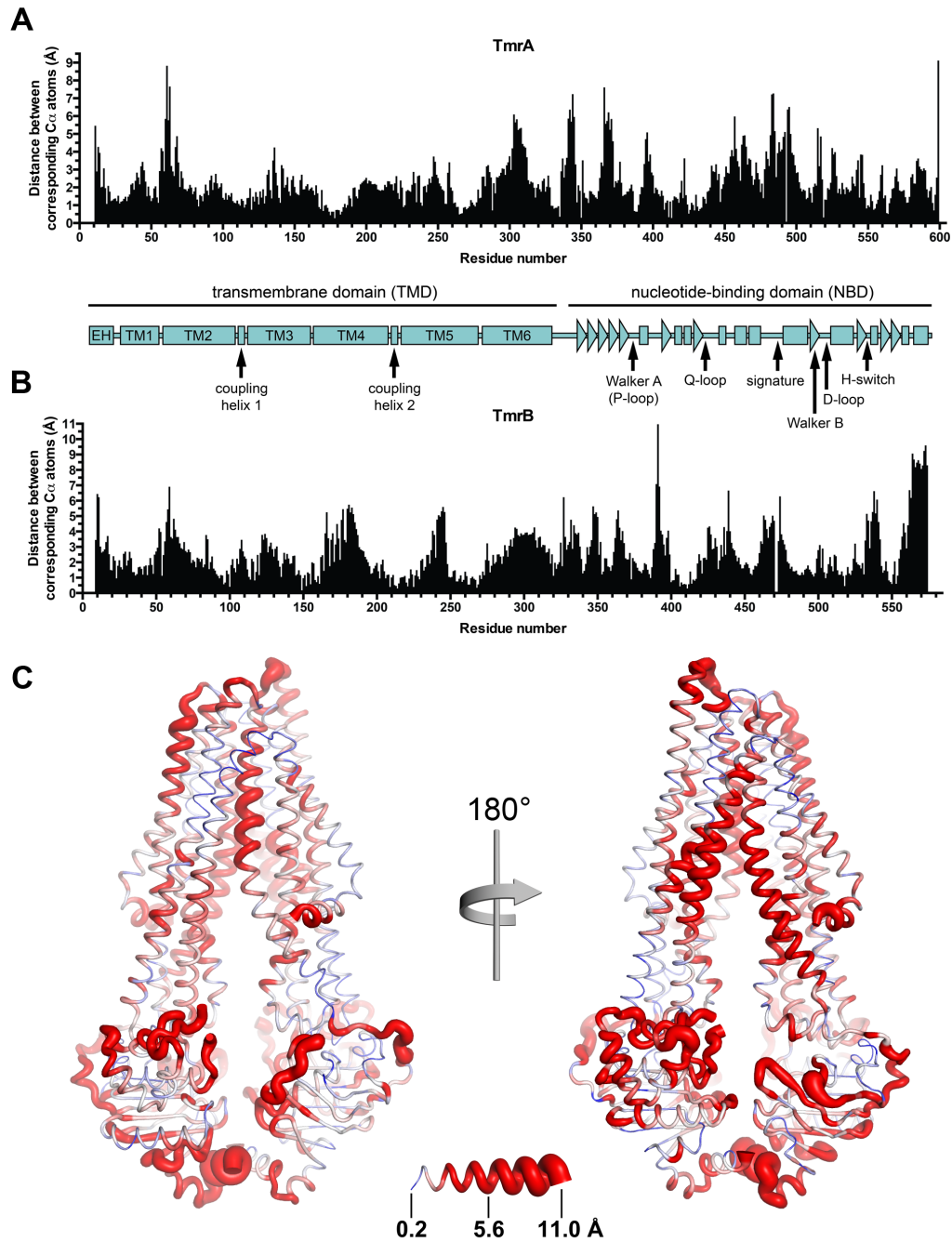
Fig. S4. Comparison of X-ray structure with cryo-EM model of TmrAB. The X-ray structure and the cryo-EM model of TmrAB were superimposed and the Cα atomic distance for each residue was calculated. (***A***) Distance plot for TmrA. The secondary structural elements are shown schematically below the plot; characteristic sequence motifs are marked. (***B***) Distance plot for TmrB. (***C***) Putty cartoon representation of TmrAB depicting the Cα atomic distances; the color spectrum blue-white-red covers a distance range of 0.2-3 Å. The correlation between cartoon thickness and atomic distance is shown at the bottom.
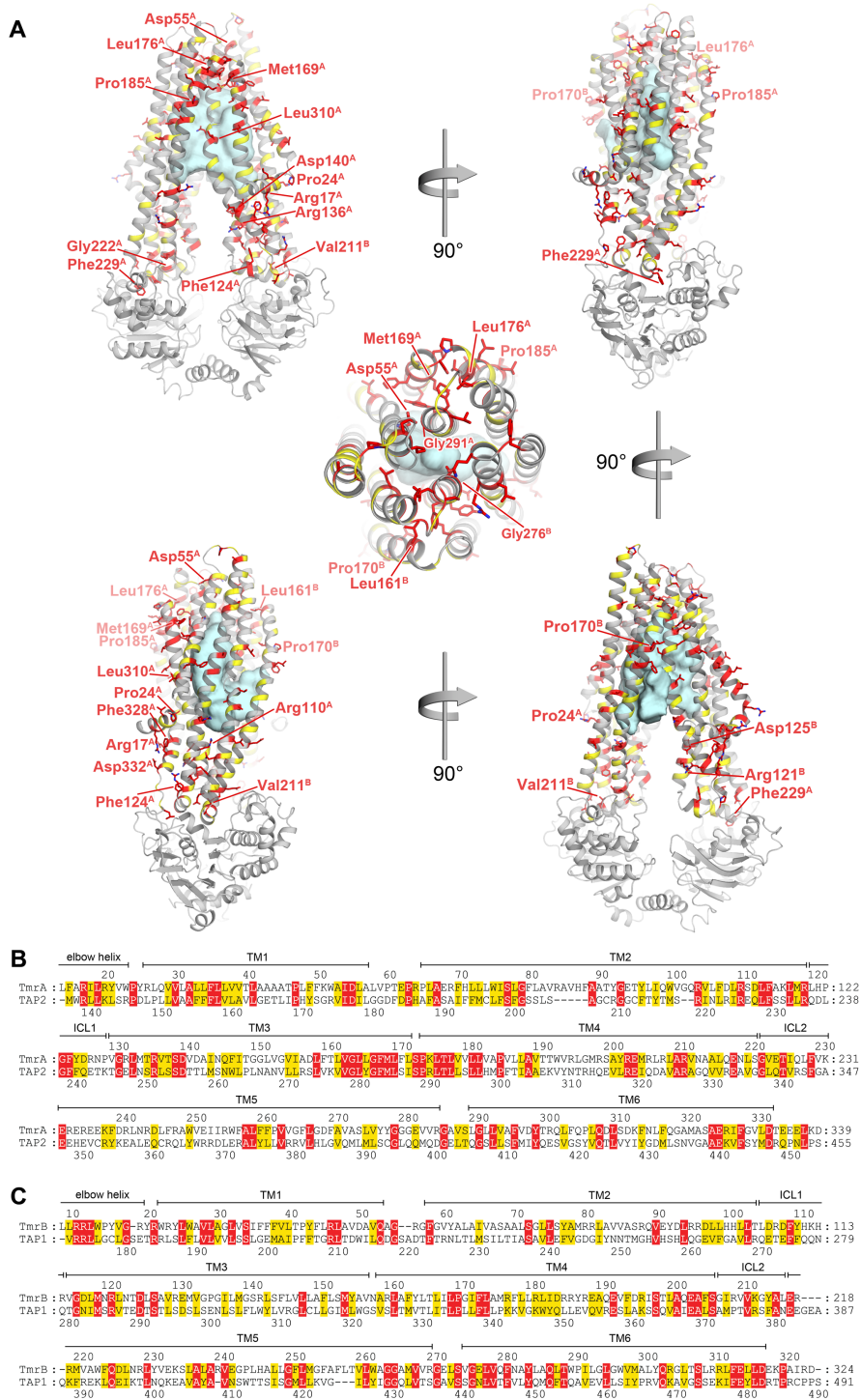
Fig. S5. Sequence conservation between the TMDs of TmrAB and TAP1/2.
Invariant residues are shown in red, physicochemically conserved residues in yellow. (***A***) Ribbon representation of the TmrAB structure in different orientations (successive rotations starting at the top left corner of the panel); invariant residues are depicted as sticks, the periplasmic gate is shown at the center of the panel. Residues that are also invariant in TM288/287, Sav1866, and MsbA, are labeled. The cavity is shown in cyan. (***B***) Sequence alignment of the TMDs of TmrA and TAP2. (***C***) Sequence alignment of the TMDs of TmrB and TAP1.
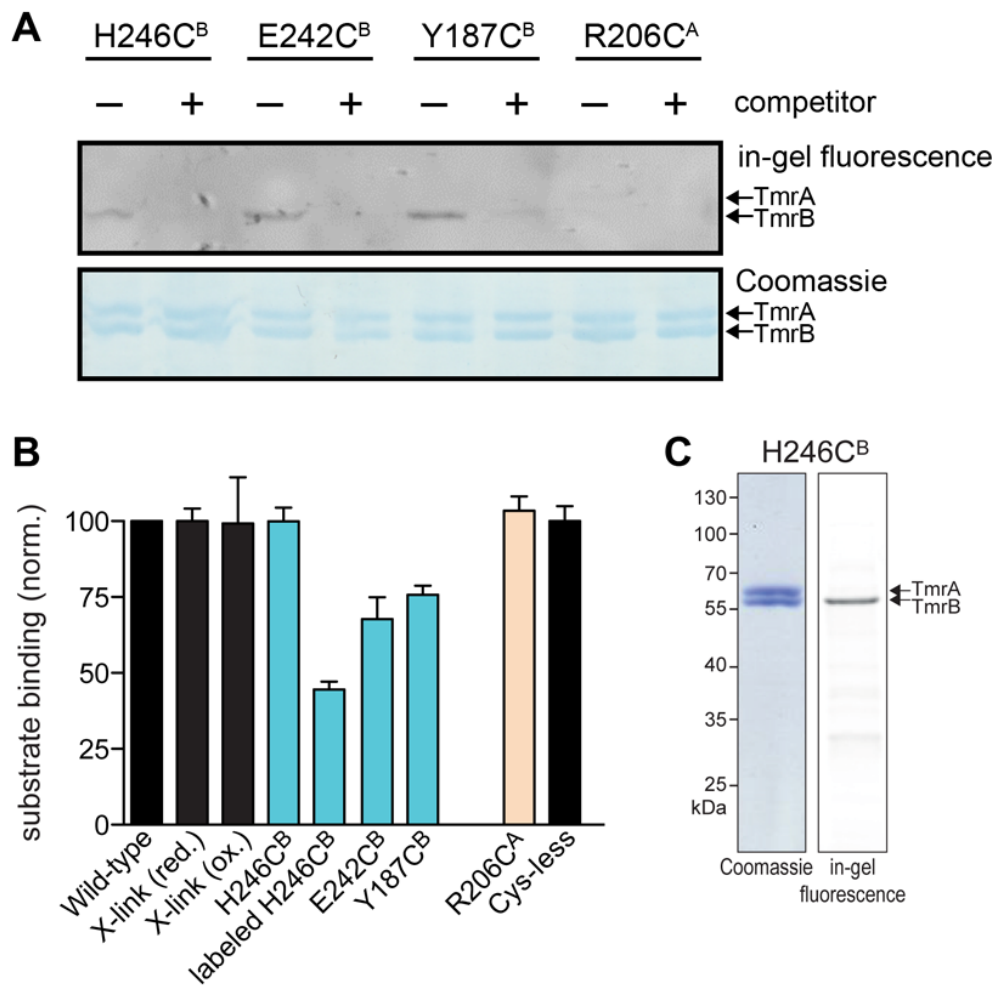
Fig. S6. Substrate binding to TmrAB. (*A*) Oxidative cysteine cross-linking of cavity-residue positions with fluorescent peptide (RRYCK[FL]STEL) containing a free cysteine; competitor: RRYC[FL]KSTEL. (*B*) Binding of [FL]peptide (50 nM) to TmrAB variants (10 µM) was followed by fluorescence polarization and normalized to the wild-type binding values. Substitutions were introduced in Cys-less TmrAB (C416A[A]), which displays the same substrate binding properties as wild-type. X-link: C416A,L595C[A]/E568C[B] under reducing (red.) and oxidizing conditions (ox.); Cys-less: TmrA[C416A]/TmrB. (*C*) H246C[B] was labeled with ATTO674N-maleimide as demonstrated by SDS-PAGE (Coomassie-stained) and in-gel fluorescence ($\lambda_{ex/em}$ 630/670 nm).
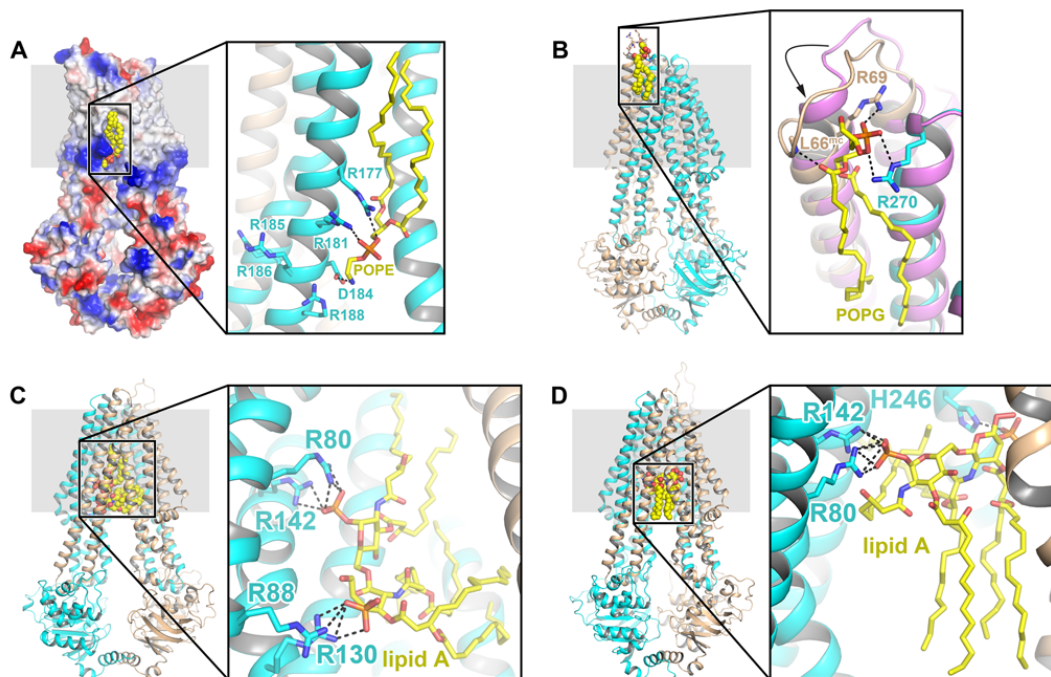
Fig. S7. MD-simulated lipid interactions with the lateral gate and periplasmic loop 1, and binding in the substrate cavity. (*A*) Interactions of a POPE molecule with the lateral gate in TmrB. In the overview, TmrAB is shown with its electrostatic surface charge. (*B*) Binding of a POPG molecule, whose anionic headgroup rigidifies the extended periplasmic loop 1 (X-ray structure shown in violet). (*C, D*) Two possible binding modes of lipid A in the substrate binding cavity of TmrAB. In most regions around the perimeter of the TMD, lipids exchanged readily on the μs timescale of the simulations. However, lipid interactions persisted in all four simulations, for POPE and POPG, with (i) the lateral gate, (ii) the nearby N-terminal arm, (iii) the symmetry-related cleft in TmrA, (iv) the TmrA N-terminal region, and (v) a cluster of arginines between TM2^B/R81^B and TM5^A/R255^A. Shown are representative snapshots of the MD simulations. TmrA in cartoon representation is shown in wheat, TmrB in cyan. Lipids are shown in yellow. Dashed lines indicate polar interactions.
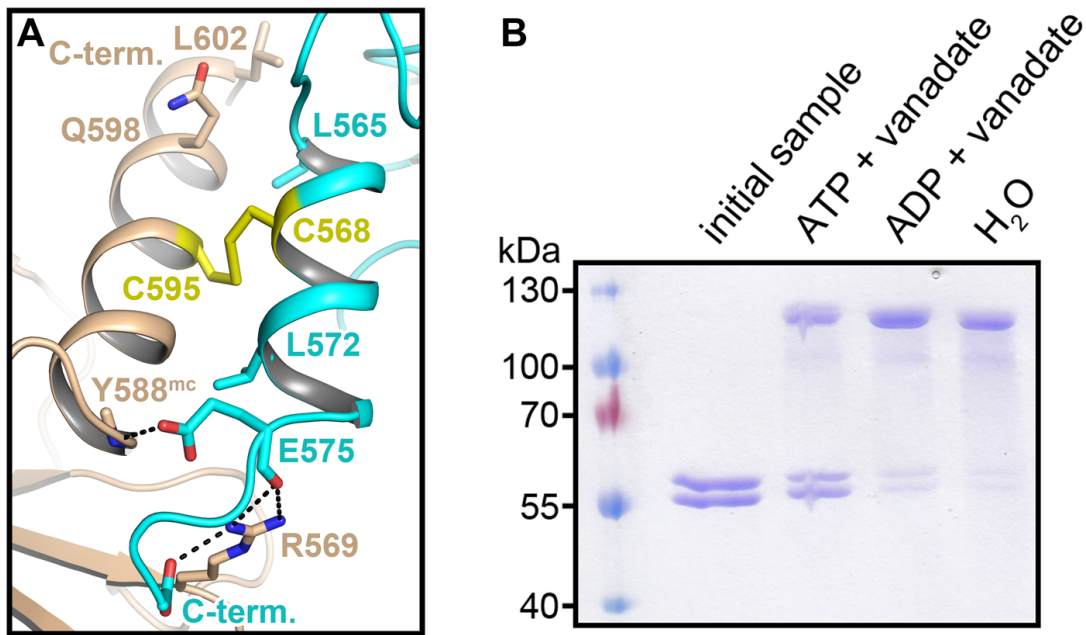
Fig. S8. Cross-linking as a probe to identify conformational changes during the catalytic cycle of TmrAB. (*A*) Model of cross-linked C-terminal zipper helices of the C416A,L595C[A]/E568C[B] mutant in the inward-facing state. The model was prepared using the program PyMOL by mutating Leu595[A] and E568[B] in the X-ray structure to cysteine. (*B*) Coomassie-stained SDS-PAGE with samples of the vanadate-trapping experiment. Cross-linking of the C-terminal zipper helices in C416A,L595C[A]/E568C[B] is less efficient when the mutant is vanadate-trapped in the presence of ATP, indicating that the zipper helices separate during NBD closure and nucleotide occlusion.
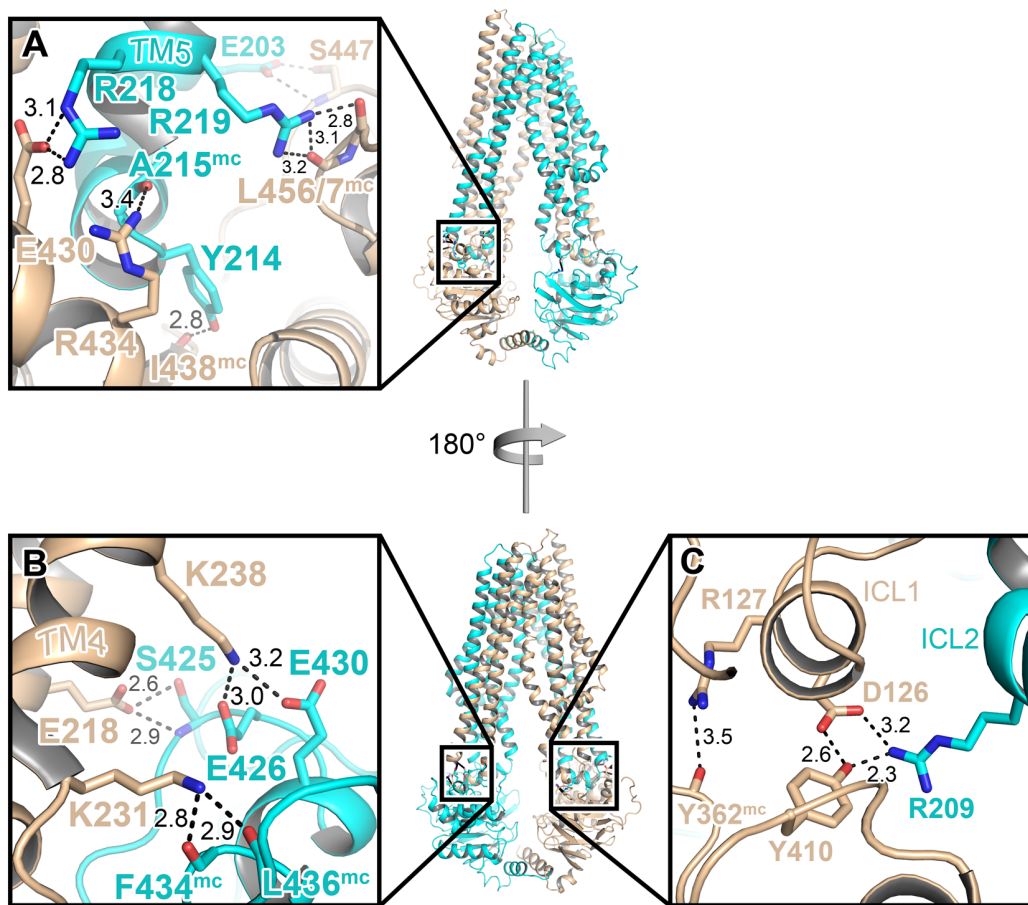
Fig. S9. Important polar interactions mediate the allosteric crosstalk within TmrAB. (*A*) Contacts between the intracellular loop 2 (ICL2) of TmrB and the NBD of TmrA. (*B*) Interactions between residues of the TmrA-ICL2 region and the NBD of TmrB. (*C*) Contacts between residues of the TmrA-TMD-NBD loop, TmrA-ICL1 and TmrB-ICL2, respectively, and the NBD of TmrA.
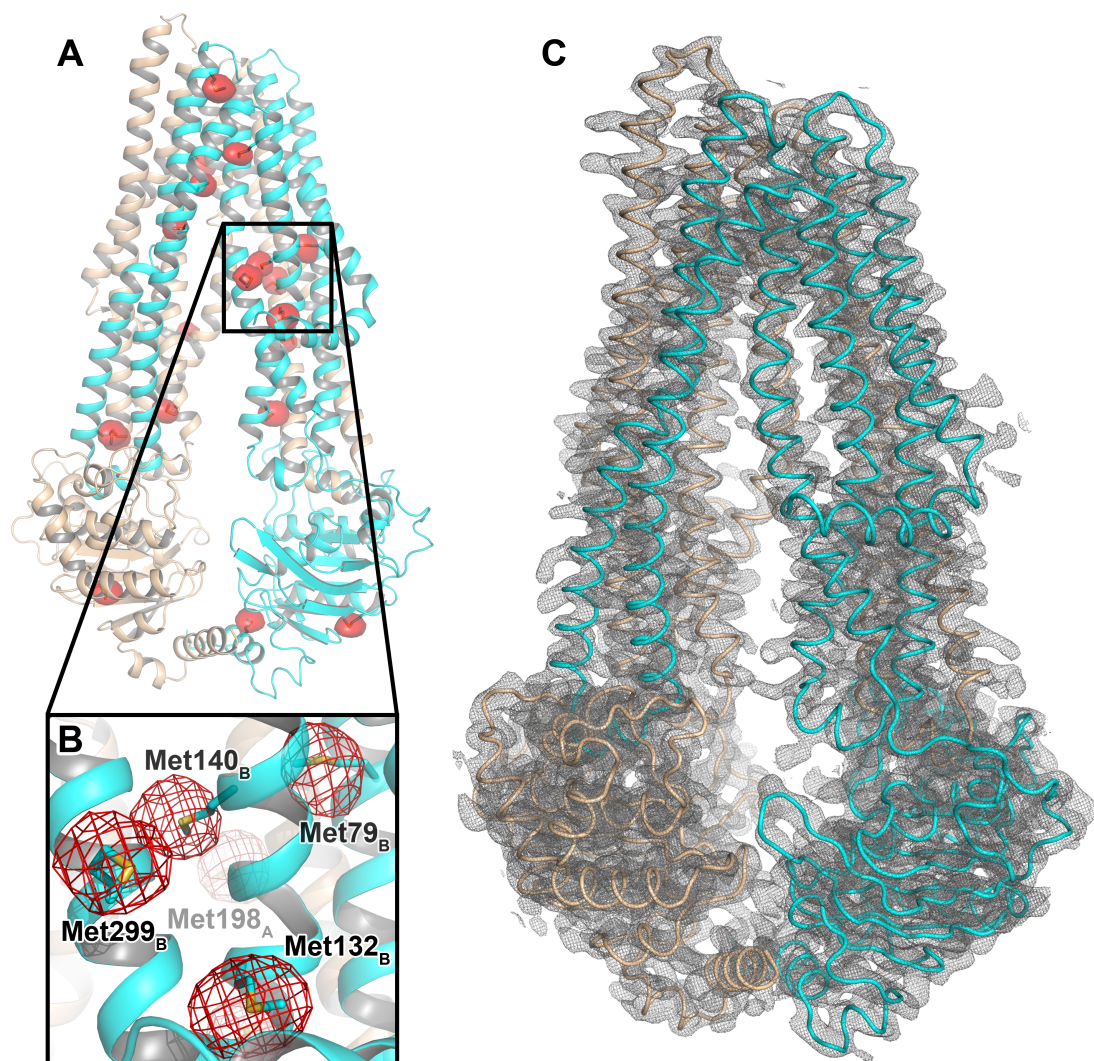
Fig. S10. Selenium-edge anomalous density and final 2Fo-Fc density map.
Selenomethionine (SeMet)-substituted protein was used to obtain phases and to guide model building. (*A*) The Se-edge anomalous density map contoured at 4σ is shown in surface representation (red) together with the model of TmrAB. (*B*) Close-up view of a model region; methionine side chains are shown as sticks, the anomalous density map is shown as red mesh. (*C*) Final 2Fo-Fc electron density map of TmrAB (contour level: 1.0σ).

Movie S1. Structural interconversion between the inward- and outward-facing conformations of TmrAB. Using PyMOL, a morph was calculated between the inward-facing structure of TmrAB and a homology model based on the outward-facing state of Sav1866. Characteristic structural elements of the NBDs are highlighted in different colors: P-loop: red; D-loop: green; signature motif: blue; Walker B: yellow; Q-loop: magenta; H-switch: orange.

Supplemental Experimental Procedures

Cross-linking of substrate with cavity residues

Purified and solubilized single-cysteine TmrAB mutants at a concentration of 1 μM were incubated in reaction buffer (20 mM HEPES pH 6.8, 150 mM NaCl, 1 mM β-DDM) at room temperature for 2 min with 5 μM fluorescein-labeled peptide containing a free cysteine (RRYCK^{FL}STEL). Control reactions were pre-incubated for 15 min with 500 μM of a fluorescein-labeled competitor peptide that lacks a free cysteine (RRYC^{FL}KSTEL). Subsequently, 12.5 μM copper phenanthroline was added and the reactions were incubated for an additional 2 min to increase cross-linking efficiency. 5 mM N-ethylmaleimide (NEM) was added to stop the reaction. The samples were supplemented with non-reducing SDS-loading buffer and analyzed by SDS-PAGE. Bands were visualized by fluorescein fluorescence using an ImageQuant LAS 4000 (GE Healthcare) and by Coomassie staining.

Cross-linking of C-terminal helices in vanadate-trapped TmrAB

Purified and solubilized TmrA^{C416A,L595C}/TmrB^{E568C} was stored in reducing buffer (20 mM HEPES pH 6.8, 150 mM NaCl, 1 mM β-DDM, 30 mM TCEP) to avoid cross-linking. To initiate vanadate trapping, 0.25 mg/ml protein was supplemented with 10 mM vanadate, 10 mM MgCl$_2$, and 10 mM ATP, ADP, or H$_2$O. The solution was incubated for 5 min at 68 °C and the reducing buffer was directly exchanged to non-reducing buffer (20 mM HEPES pH 6.8, 150 mM NaCl, 1 mM β-DDM) via a Zeba Spin Desalting Column 7K (Thermo Fisher Scientific). To induce cross-linking, CuSO$_4$ was added (10 mM final) and incubated for 1 min before the reaction was stopped by addition of 8 mM N-ethylmaleimide (NEM). The samples were analyzed by non-reducing SDS-PAGE (Coomassie stain).

Molecular dynamics simulations

We conducted extensive (5 μs) all-atom explicit solvent molecular dynamics (MD) simulations of lipid-membrane embedded TmrAB starting from the X-ray structure. According to MCCE (1) electrostatics calculations for neutral pH, all Asp, Glu, Arg, and Lys residues were charged. All histidine residues were neutral, protonated at either their Nδ or Nε atoms according to the network of hydrogen bonds, except the

charged H100[B]. Buried water molecules were added using DOWSER (2). To explore lipid effects, TmrAB was embedded (3) in a bilayer of 491 1-palmitoyl-2-oleoyl-phosphatidylglycerol (POPG) lipids (system 1) and in a bilayer of 518 1-palmitoyl-2-oleoyl-phosphatidylethanolamine (POPE) lipids (system 2). Both systems were hydrated with 150 mM NaCl electrolyte in a simulation box of ~13×13×16.5 nm^3. Consistently in all simulations, we used the all-atom CHARMM36 force field for TmrAB, lipids, and ions, together with TIP3P water (4-6). The parameters for lipid A were taken from Wu *et al.*(7). The MD trajectories were analyzed with Visual Molecular Dynamics (VMD) (8).

Simulations were performed using the NAMD 2.9 (9) and GROMACS 4.6 (10) simulation packages, taking advantage of their different functionalities and computational speeds. A first set of MD simulations of the two systems was performed using NAMD 2.9. After 10,000 steps of conjugate gradient energy minimization, 10 ns of MD simulation was carried out in which all non-hydrogen atoms of the protein were constrained to their initial positions using springs with progressively smaller force constants, starting at 15 $kcal·mol^{-1}·Å^2$. Analysis was carried out on unconstrained simulations, each 0.5 μs long. Periodic boundary conditions were used, with particle-mesh Ewald electrostatics, a 1.2 nm non-bonded cutoff, a time step of 2 fs, SHAKE constraints on all bond lengths, and a constant temperature of 310 K maintained by a Langevin thermostat with a coupling coefficient of 1.0 ps^{-1}. A Nosé–Hoover Langevin barostat was used to apply constant pressure of 1 bar normal to the membrane plane. The box shape in the x-y membrane plane was kept fixed. A second set of simulations was performed using GROMACS 4.6. The starting systems were minimized for 50,000 steps with steepest descent energy minimization and equilibrated for 100 ps in the NVT ensemble, then 10 ns of MD simulation in the NPT ensemble was carried out in which all non-hydrogen atoms of the protein were restrained to the fixed reference positions with progressively smaller force constants, starting at 4000 $kJ·mol^{-1}·nm^2$. Analysis was carried out on unconstrained simulations, each 2 μs long. Periodic boundary conditions were used. Particle-mesh Ewald with cubic interpolation and a 0.16 nm grid spacing was used to treat long-range electrostatic interactions. The time step was 2 fs. The LINCS algorithm was used to fix all bond lengths. Constant temperature (310 K) was set with a Nosé-Hoover thermostat, with a coupling constant of 0.5 ps. A semi-isotropic

Parrinello-Rahman barostat was used to maintain a pressure of 1 bar. All simulations with lipid A bound to TmrAB were performed using NAMD 2.9 following a similar protocol as described above. A lipid A molecule was placed in the substrate-binding cavity in several random orientations and after the equilibration runs, each run was extended for 30-50 ns. After identifying two distinct binding modes, two snapshots from the initial runs were used as the starting points for new runs of 120 ns duration. In the binding mode with the headgroup pointing upward, both H246[B] and H87[A] were assigned to be charged.

Supplementary References

1. Alexov EG & Gunner MR (1997) Incorporating protein conformational flexibility into the calculation of pH-dependent protein properties. *Biophys J* 72:2075-2093.

2. Zhang L & Hermans J (1996) Hydrophilicity of cavities in proteins. *Proteins* 24:433-438.

3. Wu EL, *et al.* (2014) CHARMM-GUI Membrane Builder toward realistic biological membrane simulations. *J Comput Chem* 35:1997-2004.

4. Best RB, *et al.* (2012) Optimization of the additive CHARMM all-atom protein force field targeting improved sampling of the backbone phi, psi and side-chain chi(1) and chi(2) dihedral angles. *J Chem Theory Comput* 8:3257-3273.

5. Jorgensen WL, Chandrasekhar J, Madura JD, Impey RW, & Klein ML (1983) Comparison of simple potential functions for simulating liquid water. *J Chem Phys* 79:926.

6. Klauda JB, *et al.* (2010) Update of the CHARMM all-atom additive force field for lipids: validation on six lipid types. *J Phys Chem B* 114:7830-7843.

7. Wu EL, *et al.* (2013) Molecular dynamics and NMR spectroscopy studies of *E. coli* lipopolysaccharide structure and dynamics. *Biophys J* 105:1444-1455.

8. Humphrey W, Dalke A, & Schulten K (1996) VMD: visual molecular dynamics. *J Mol Graph* 14:33-38, 27-38.

9. Phillips JC*, et al.* (2005) Scalable molecular dynamics with NAMD. *J Comput Chem* 26:1781-1802.

10. Hess B, Kutzner C, van der Spoel D, & Lindahl E (2008) GROMACS 4: algorithms for highly efficient, load-balanced, and scalable molecular simulation. *J Chem Theory Comput* 4:435-447.